ANALYZING SURFACE DEFORMATION USING INSAR & OTHER REMOTE SENSING DATA IN THE OLKARIA GEOTHERMAL FIELD & SURROUNDING AREA, KENYA

FITRIANI AGUSTIN
February, 2012

SUPERVISORS:
Dr. Tsehai Woldai
Dr. Valentyn Tolpekin

ANALYZING SURFACE DEFORMATION USING INSAR & OTHER REMOTE SENSING DATA IN THE OLKARIA GEOTHERMAL FIELD & SURROUNDING AREA, KENYA

FITRIANI AGUSTIN
Enschede,The Netherlands, February, 2012

Thesis submitted to the Faculty of Geo-Information Science and Earth Observation of the University of Twente in partial fulfilment of the requirements for the degree of Master of Science in Geo-information Science and Earth Observation.
Specialization: Applied Earth Sciences

SUPERVISORS:
Dr. Tsehai Woldai
Dr. Valentyn Tolpekin

THESIS ASSESSMENT BOARD:
Prof.Dr. F.D.(Freek) van der Meer (Chair)
Dr. Mike Buxton (External Examiner, University of Delft, Department of Geotechnology, Civil Engineering & Geosciences)

ABSTRACT

Surface deformation can cause many problems. The study area, located in the Olkaria Geothermal Field (OGF), and its surrounding, is situated in the central Kenya rift valley, associated with an active tectonic regime in the continental rift floor. The geothermal exploitation, the groundwater extraction and the active faults segments and volcanoes are prominent features which might lead to the surface deformation in the study area.

Multitemporal Envisat ASAR data from 2003 to 2008 were used to map the ground surface displacement along the line-of-sight (LOS) direction using two InSAR approaches; two-pass differential interferogram (DinSAR) and the stacking interferogram small baseline subset (SBAS). SRTM DEM was utilized to interpret the surface active faults. ASTER VNIR FCC band 321 was used to extract the land use features along the study area. Fieldwork was carried out to validate the active surface faults and collecting secondary data on geothermal parameter.

Only one pair of interferogram from the two-pass differential interferogram (DinSAR) was used to analyze the surface deformation (2007-2008), while the rest were slightly dominated by noise. SBAS technique was used to map the surface deformation rate on the study area (2003-2008).

The surface deformation rate recorded at OGF is around 14 mm/year of uplifting and -13 mm/year of subsidence. The trending deformation pattern was coincidently bounding with the NE&NNE faults in the OGF, which possibly can be used to identify the geothermal source within unexplored areas. The injection wells activities and the structural behavior might contribute to the surface deformation in OGF.

The relative subsidence around Lake Naivasha occurred at about -7 to -10 mm/year which was coincided with the horticulture agriculture activities. Decreasing trends on the groundwater level measurement within the agriculture areas confirmed with the subsidence pattern in the two wells (e.g., Boinnet BH1 & Boinnet BH2). Groundwater extraction possibly leads to the surface deformation around Lake Naivasha.

The slow subsidence about 28 mm was detected using one interferogram pair (2007-2008) associated with the active faults in the Kenya rift floor. Slight vertical displacement recorded at about 6 mm associated with the N-S trending fault. SBAS stacking interferogram (2003-2008) detected the activity of Mt. Longonot, located in the southeast of Lake Naivasha, shows uplifting in the range of 5 to 15 mm/year.

The stacking interferogram using small baseline subset (SBAS) technique is able to map multi-temporal slow rate surface deformation in the study area. However, conventional two-pass differential interferogram (DinSAR), could not be applied properly. The decorrelation effects in longer time acquisition, natural effects such as atmospheric and seasonal condition and other technical effect might contribute during SAR images selections and processing. The integrated surface deformation map with the active surface faults and other secondary dataset are able to identify the cause of deformation in the three main features activities in the study area.

ACKNOWLEDGEMENTS

In the name of God, Most Gracious, Most Merciful. My highest gratitude is only for Allah Who creates a universe.

I would like to express my gratitude to the Netherlands Education Support Office (NESO) Indonesia, for granted me to study through STUNED Scholarship Program.

I would like to thank to Geological Agency, Ministry of Energy and Mineral Resources, Indonesia, for allowing me to take a leave for study in ITC.

I am grateful to my supervisors, Dr. Tsehai Woldai and Dr. Valentyn Tolpekin, for being encouraging during my thesis part, and for all scientific and critical comments.

I am thankful to Dr. Paolo Pasquali, Technical Director Sarmap s.a., for giving me an opportunity to use a temporary license on SARScape Interferometry stacking.

I am thankful to European Space Agency (ESA) for providing me the Envisat ASAR dataset for my observation.

My sincere gratitude to Dr. Geoffrey G. Muchemi, Geothermal Development Manager Olkaria Geothermal Project, Kenya Electricity Generating Company Ltd. (KenGen), for allowing me to do data collection and field visit in the Olkaria Geothermal Field, Naivasha, Kenya. I express thanks to my dear Wesley Koros, for accompany me during fieldwork and discussed the funny things in Swahili. To Drs. Robert Becht, thanks for arrange everything for being comfortable while I was in the field.

I would like to thank to Drs.Tom Loran, Dr.D.G.(David) Rossiter and Drs.J.B.(Boudewijn) de Smeth and all ITC staff for their kindness and friendly during my study time. Special thanks to Run4Fun (Wan Bakx, Simon, and the team) for sharing the running experiences and “escape” from PC-based work environment.

To my fellow AES-ERE students, Abweny, Kamina, Sharah, Chandima, thanks for a great friendship and caring during the study time.

I must thanks to ITC Indonesian Community; Iday, Rani, Idham, Arie, Doddy, Fesly, Mba Tiur, Debi, Nunos, Pa Syarif, Pa Anas, Pa Win and Bu Dewi, for sharing the joys and being around during the hard time.

Finally, I would like to thank to my husband, Wahyudi, for being patience and endless motivating me. To my parents, brothers and sisters, thanks for all the pray and valuable supports.

Enschede, February 2012

Fitriani Agustin

TABLE OF CONTENTS

LIST OF FIGURES

LIST OF TABLES

1. INTRODUCTION

1.1. Background

Demand for clean and renewable energy worldwide has been increasing over the years. According The World Energy Council estimation, the renewable energy sources will provide 20–40% of the total world energy consumption in 2050 and 30–80% in 2100 (Bertani, 2005). This picture is influenced by several factors such as the scarcity of fossil fuels, the increasing concern on reducing greenhouse gases emission, and the growth of energy consumption.

Geothermal energy source ranks as the third renewable energy used for electricity generation after hydropower and biomass (Fridleifsson, 2001). Current figure in 21st century, at least the four developing countries energy produced more than 10% of their total electricity from geothermal (El Salvador 18%, Kenya 11%, Nicaragua 18% and Philippines 21%). These numbers are followed by the increase on the geothermal power plant installations (Fridleifsson & Freeston, 1994).

In Kenya, the geothermal power plant installation in Kenya increased about 185 % in 2005. It was very significant one if compare this to Indonesia and Mexico which produced 35% and 25% at the same period (Bertani, 2005). In addition to that figure, the Kenya Government plans to increase the installation geothermal power plant to expand to 1500 MWe and 4000 MWe by 2018 and 2030 (Simiyu, 2010). This action is supported by the fact that the country is endowed with 7000 MWe of potential geothermal energy enough to supply the country energy demand for the next 25 years (Simiyu, 2010). As a result, more exploration and development project are underway in the area surrounding the current active geothermal fields or in prospective areas.

Geologically, the current Kenyan geothermal fields operate mainly along the Kenya Rift Valley (KRV) associated with young active Quaternary volcanic centres such as Mt. Suswa, Mt. Olkaria, Mt. Longonot, Mt. Eburru, Mt. Menengai and along active faults related to the continental rift floor, e.g. Magadi, Bogoria, Arus, Baringo and Kapedo fields (Riaroh & Okoth, 1994).

Olkaria Geothermal Field (OGF), situated in the axial of central KRV, is the most productive power plant in Kenya. The total production in 2009 rich to 169.8 MW which divided into sub-fields; Olkaria I (east) 45 MW, Olkaria II (NorthEast) 70 MW, Olkaria III (West) 48 MW, Olkaria IV (West - binary) 1.8 MW and Oserian plant 2 MW.

Close to OGF, there are many agricultural based industries which are very dependent on the groundwater abstraction and surface water demand from the lake close by, Lake Naivasha (Becht & Nyaoro, 2005). Groundwater and surface water from the lake have been extracting since 1940s and it continues to increase in 1980s as flower industries have grown successfully on supplying roses for European Market. Nowadays, all part of the areas surrounding Lake Naivasha has been occupied by these flower farms and possibly to extent in future.

In addition, the presence of active volcano Mt. Longonot and dissected active normal faults across the OGF, Lake Naivasha and surrounding areas, creates this area as a significant place influenced by tectonics within KRV zones (Chorowicz, 2005).

1.2. Problem statement

During the geothermal exploitation stage, the surface deformation in a geothermal field is a common problem due to reservoir pressure reduction. As a consequence, it will decrease the reservoir compressive strength that will lead to subsidence on reservoir overlaying strata. Furthermore, when it reaches shallow groundwater aquifer, simple dehydration due to shrinkage of clay deposits will occur. This condition is expected to occur in OGF, Kenya. Oduor (2010) reported that there is no subsidence related to the surface deformation being investigated in Olkaria Geothermal Field until now.

Moreover, the exceed on groundwater withdrawal in the northern part of Lake Naivasha and surrounding, have caused the significant depletion on groundwater level up to 6 meter down from the previous normal water table as reported by Becht & Nyaoro (2010).

Apart from the geothermal exploitation and groundwater abstraction, geodynamic activities resulting from active fault systems within the KRV might contribute to the local surface deformation over the field. Kuria, et al. (2010) investigated the active fault segments in the Magadi Area (south of the current study area), using subsurface geophysical and remotely sensed data and their findings show active faults are contributing to earthquake potential in the area related to the magmatic intrusion within the continental rift system.

The integrated approach of monitoring geothermal exploitation, geodynamic activities and other man-made activities such as groundwater extraction are limited. This research, therefore, aims to integrate these factors to insight the surface deformation over the Olkaria Geothermal Field and surrounding areas.

1.3. Research motivation

Challenges from theoretical Interferometric SAR (InSAR) into practical application have been numerously tested for surface deformation mapping by several researchers.

In nature induced surface deformation, InSAR is able to detect crustal deformation due to an earthquake during seismic event. Through this method, the earthquake deformation is detected along rupture zones parallel to the main fault. Such works have been tested in major earthquake fault related in some areas, e.g Bam (Iran), Italy and Greece (Goudarzi, 2010; Stramondo et al., 2005). By combining InSAR measurement with deformation observation from reference data (GPS), the result is able to optimize crustal deformation studies (Chlieh et al., 2004; Wei et al., 2010). InSAR for monitoring deformation rate in volcanic activities are also known from the work of Samsonov S. et al. (2009) and Han et al. (2010).

InSAR studies in anthropogenic deformation have been applied to various volume changes on earth surface due to man-made activities. For example, identifying land subsidence within the densely populated cities caused by groundwater extraction (Glowacka et al., 2010; Ketelaar, 2009), mining induced subsidence (Woldai et al., 2009; Zhao et al., 2011) and deformation monitoring on geothermal exploitation (Chang et al., 2005; Fialko & Simons, 2000; Hole et al., 2007; Samsonov S., et al., 2009).

In geothermal field, InSAR technique provides a unique opportunity to infer cm scale earth surface deformations induced by the gases and liquids extraction during heat production. It also appears to provide valuable new information on the extent of the reservoir system beyond the known field and possible on the effectiveness of reinjection wells and natural recharge. It is more effective when compared to conventional geodetic method that possibly needs expensive labors and equipments maintenance. Furthermore, it allows for accurate detection (up to 1 cm scale) of surface deformation (Fialko & Simons, 2000). The combination of surface deformation results obtained through the analysis of InSAR data with observation from reservoir production wells will assist in the exploration of geothermal fields and reservoir production management.

1.4. Research objectives

The main objective of this research is to investigate the surface deformation related to geothermal exploitation, groundwater extraction, or tectonic activities over the Olkaria geothermal field and its surrounding area. To reach the main objective, the specific objectives are listed as follow:

- To map the surface deformation in the Olkaria geothermal field and surrounding using InSAR approach
- To identify the source/causes of deformation in Olkaria geothermal field
- To identify the cause of deformation around Lake Naivasha
- To identify the cause of deformation related to the tectonic activities within the central Kenya rift system

1.5. Research questions

In order to reach the objectives, the research will try to answer these questions:

- Is the technique robust enough to determine where surface deformation could have occurred?
- Can the sources for surface deformation 1) in the Olkaria Geothermal field, 2) around Lake Naivasha and 3) those related tectonic activities be determined using InSAR techniques?

1.6. Hypothesis

1. Surface displacement up to millimeter scale change can be detected using InSAR
2. The reduction of pressure due to pumping in geothermal fluid lead to surface deformation since the reservoir compressive strength become less
3. Excess in groundwater abstraction will lead to the vertical ground motion
4. The rupture zones over active fault are potential to cause surface displacement

1.7. Thesis outline

The outline of thesis will be described as follow:
Chapter 1 outlines the background to the research, problem statement, research motivation, objectives, research questions and hypothesis.
Chapter 2 describes the brief overview of the study area including the regional geology and tectonic setting, local geology and structure of Olkaria Geothermal field, and the previous works on regional deformation studies in Kenya Rift Valley.
In Chapter 3, the dataset were used and the methods applied in processing various dataset were discussed.
In Chapter 4 the result on surface deformation from InSAR, surface active fault interpretation from DEM SRTM including its fieldwork validation and the agriculture feature extraction through ASTER image were described.
Chapter 5 discusses on data integration and analysis of ground surface deformation related to geothermal exploitation in the Olkaria Geothermal Field, groundwater extraction surrounding Lake Naivasha and recent tectonic activities in the central Kenya Rift Valley.
Finally, Chapter 6 is on conclusion and recommendation

2. STUDY AREA

In this chapter, a brief explanation of the regional physiography, geology and tectonic condition of the Olkaria Geothermal Field and its surroundings is provided. Description on the works is from previous researchers. Those are compiled by the author to obtain general ideas of the regional condition over the study area. In terms of local interest, the further explanation of the local geology and historical production in OGF together with the current figures on groundwater abstractions surround Lake Naivasha are also discussed.

2.1. Physiography

Geographically, the study area is situated in the floor of East African Rift Valley, Naivasha area which is approximately 100 km North-West from the capital city of Kenya, Nairobi. The rift valley climate is generally considered semi-arid with an annual rainfall is around 650 mm.

The general altitude in the study area ranges from 1900 m in the rift floor to around 2700 m in the western and eastern rift border. Administratively, the study area is part of the Rift Valley province with its previous capital city Nakuru district that recently moved to Naivasha town. The main road passed across the city of Naivasha linking Mombasa-Nairobi-Naivasha-Nakuru. The three main activities were concerned within this study area; Olkaria Geothermal Field (OGF), Lake Naivasha, Agricultures and active volcano as part of Kenya rift valley system (figure 2.1).

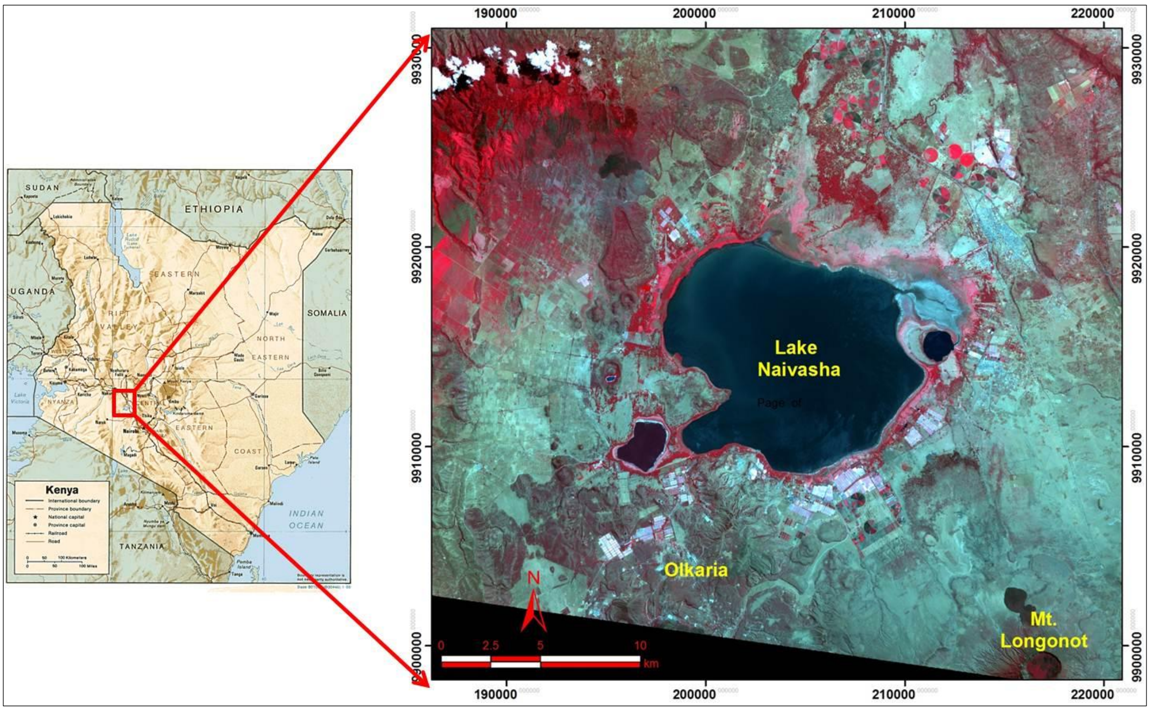

Figure 2.1: Map of Kenya (*www.nationmaster.com*) (left). The study area (right) is an ASTER false colour composit (FCC) 321 (in RGB mode) image showing the main activities of Olkaria Geothermal Field, Lake Naivasha, agricultures, and active volcano in the central Kenya rift valley.

2.2. Regional geology and tectonic setting

Figure 2.2 illustrates the regional geology map modified from Thompson and Dodson (1967) and published by The Geological Survey of Kenya. SRTM (90m) resolution is overlaid to highlight the terrain and lithological composition of the area. As shown in Figure 2.2, most of the area is dominated by recent Quaternary volcanic products and it mixed with lacustrine sediment deposited near the end of the Pleistocene period (light yellow areas) spreading along the edge of Lake Naivasha. The detail description of each lithological unit is shown is figure 2.2 and described in table 1.

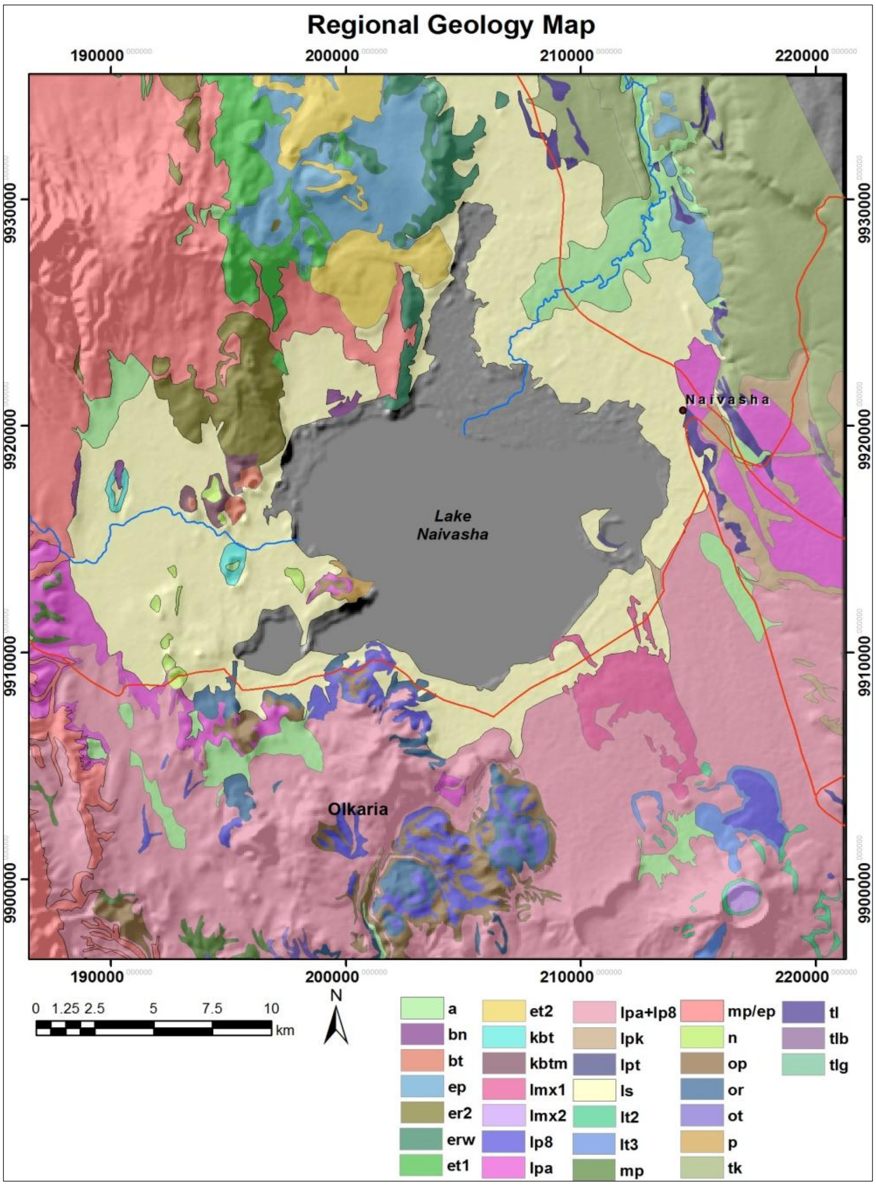

Figure 2.2: Regional geology of central Kenya rift valley. Olkaria geothermal field is situated at Southwestern part of the map (modified from Thompson & Dodson, 1967).

Table 1: The description of lithology unit from regional geology map of Lake Naivasha in figure 2.2 (Modified from Thompson & Dodson 1967)

Litho Unit	**Lithology Description**
a	Alluvial deposit
bn	Ndabibi basalt,hawaiite lava flows,pyroclastic cones
bt	Surtseyan/strombolian ash cones
ep	Eburru pumice,pantellerite,trachytic pumice,ash fall deposits
er2	Eastern eburru pantellerite,welded and un-welded pyroclastics
erw	Waterloo ridge pantellerite,lava flows and pyroclastics
et1	Older eburru trachyte,lava flows and pyroclastic cones
et2	Younger eburru trachyte,lava flows and pyroclastic cones
kbt	Surtseyan tuff cones
kbtm	Surtseyan tuff cones with laterally equivalent fall tuffs
lmx1	Lower longonot mixed basalt/trachyte lava flows and pyroclastic cones
lmx2	Upper longonot mixed basalt/trachyte lava flows and pyroclastic cones
lp8	Longonot ash
lpa	Longonot Olkaria pumice
lpa+lp8	Longonot ash and Olkaria pumice
ls	Lacustrine sediments
lt2	Lower trachyte ignimbrites and associated fall deposit
lt3	Upper longonot trachyte,lava flows and pyroclastic cones
mp	Maiella pumice,trachyte,pantellerite pumice and ash fall deposits
mp/ep	Maiella pumice/trachyte pumice
n	Ndabibi comendite lava flows,domes and pyroclastics
op	Olkaria comendites,pyroclastics (include pre-lpk lacustrine sediments,reworked pyroclastics in ol Njorowa gorge
or	Olkaria comendites,lava flows and domes include Njorowa pantellerite lava and welded pyroclastics
ot	Olkaria trachyte,lava flows
p	Ndabibi pantellerite lava flows
tk	Kinangop tuff (eastern rift margin)
tl	Limuru trachyte
tlb	Karati and ol mogogo basalt
tlg	Gilgil trachyte

Study area is situated in the central Kenya Rift Valley which is part of East African Rift System (EARS). The rift activities started in the early Miocene followed by basaltic and phonolitic volcanism. In the late Miocene, the rift faulting began and it was followed by the eruption of high volume of ignimbrite deposit within the central rift segment during Pliocene (Omenda, 1998). The rift faulting remains active until now. Recent volcanic activities are represented by Mt. Suswa, Mt. Longonot and Mt. Olkaria that are closely related to the current geothermal fields. Kenya rift valley associates with major faults along the rift boundaries trending approximately in N-S direction. It is believed to be correlated with the crustal opening in the E-W direction (Strecker et al., 1990) (figure 2.3).

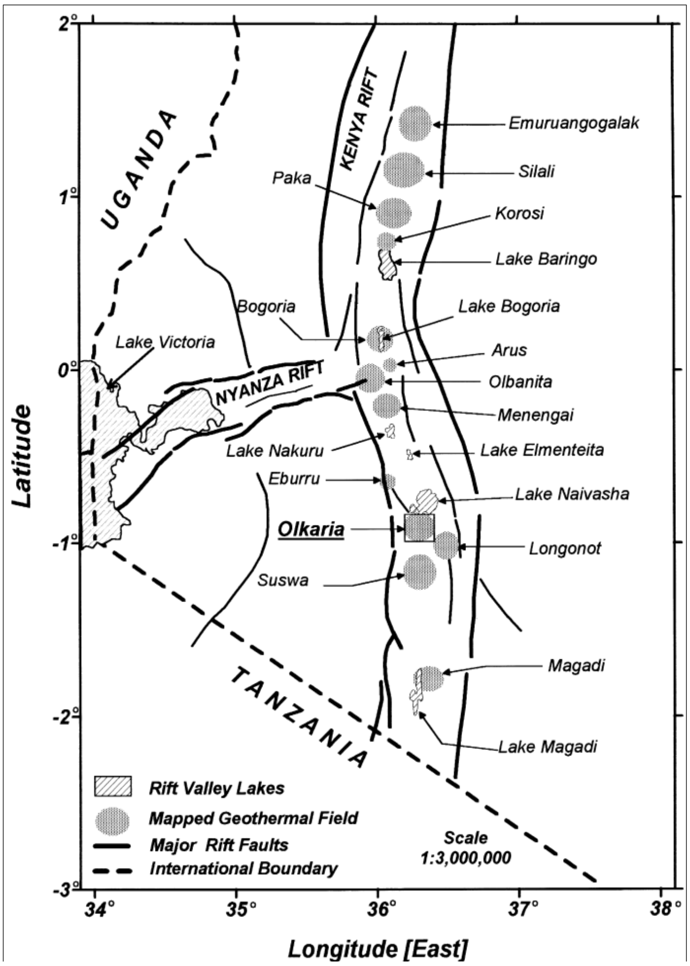

Figure 2.3: The regional tectonic pattern of Central Kenya Rift Valley, associated with major rift faults and potential geothermal field (Simiyu & Keller, 2001).

2.3. Olkaria Geothermal Field (OGF)

Geological and geophysical observations in the Olkaria Geothermal Field have been carried out by several workers (Mariita, 2000; Muchemi, 1999; Omenda, 1998; Simiyu & Keller, 2000) to obtain the obvious path flow model for geothermal system in Olkaria Geothermal Field.

2.3.1. Local geology and structure

The Olkaria volcanic complex is the main lithology covered within the OGF. It is referred as the old caldera complex composed of extrusive rhyolitic rocks and pyroclastic pumice which is cut by relatively N-S normal faults as now outcrops in Ol Njorowa Gorge (see figure 2.4). The youngest volcanic lava comprises the Ololbutot lava dating back to 180±50 yr BP (Clarke et al., 1990). The rhyolitic rocks covering the area started around 400,000 years ago (Omenda, 1998) and is marked as the most recent volcanic activities in the Olkaria Hill from where the geothermal field acquired its name. These latest magmatic activities are believed to be responsible for shallow magmatic heat source for OGF. The deep magmatic heat source might have been larger than the current old caldera complex (Omenda, 1998).

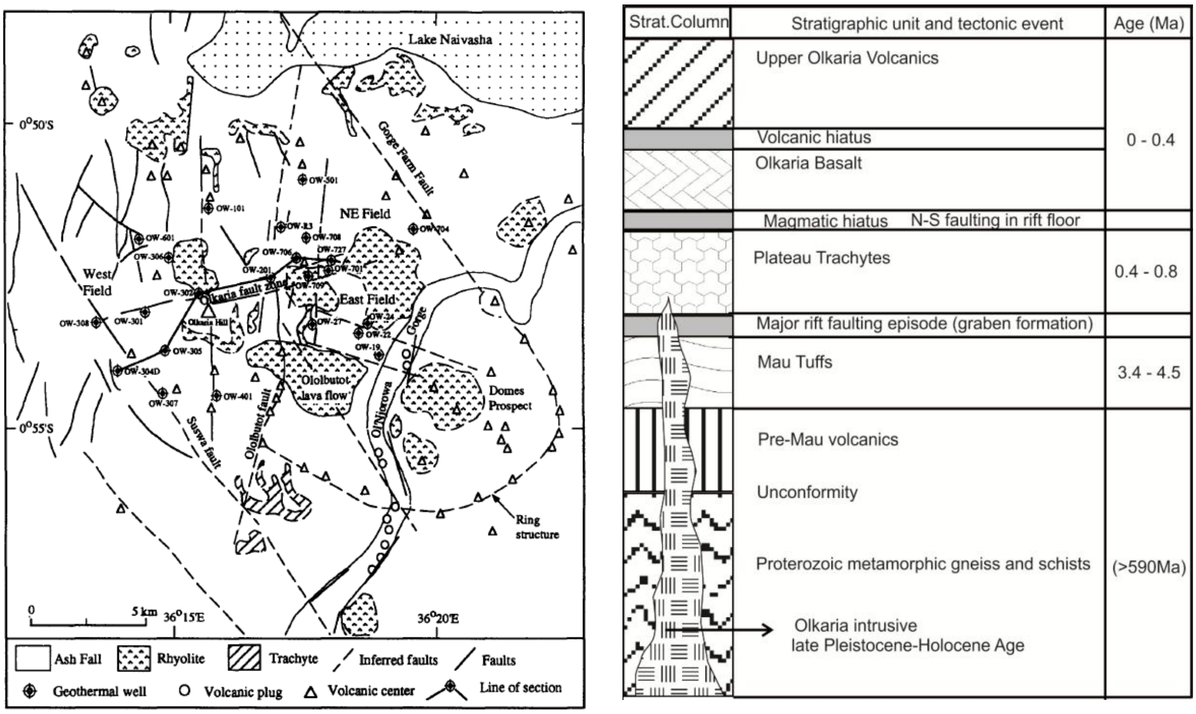

Figure 2.4: Simplified surface geology map of Olkaria geothermal field (taken from satellite imagery and previous regional geology mapping (left) and Local stratigraphy of Olkaria Geothermal Field (right). (modified after Omeda, 1998)

The stratigraphy unit of the area surrounding the Olkaria Geothermal site (figure 2.4) can be described from young to old as follow:

1. Upper Olkaria volcanics
   This comprises of comendites, pyroclastics, trachytes, and minor basalts. The comendites outcrops along the Ol'Njorowa gorge (Hell's Gate) and forms ring domes called Dome prospect in eastern Olkaria (figure 2.4). Comendites are the dominant lava within Olkaria and type locality of this lava spreads in the whole Kenya Rift Valley. It represents the latest volcanic activity in Olkaria hill, the area around Ololbutot volcanic line and Gorge Farm areas. Petrologically, the unit is similar with Plateau trachyte formation except for the modal quartz presence which is higher (74-76%), showing that this unit is strongly alkaline with Al_2O_3 (12%) and low MgO content (<0.1%).
2. Olkaria Basalt
   The Olkaria basalt overlies the Plateau Trachyte in the eastern and north eastern part Olkaria field at 1000 – 1500 m elevation and it is not apparent in the western part. It consists mainly of thin basaltic flows and minor thin tuffs layers, trachytes, and rhyolites. The thickness varies between 100-400m. The basalt is slightly vesicular, porhyritic and comprises of augite, plagioclase, and some opaque minerals in its phenocrysts, fine grained matrix and microcrystalline. The unit is moderate to highly altered as indicated by presence of clay, calcites and epidotes.
3. Plateau Trachytes
   This extrusive volcanic rock occurs in the eastern part of Olkaria and extents to the south of Mt.Suswa and to the north of Mt. Eburru. Petrographic studies of this unit taken from bore hole, suggest that it consist of two types of trachyte; 1). Un-altered feldspar trachyte which is dense, brownies grey, porphyritic, and consist of phenocrysts of sanidine (up to 5 mm in length). 2). Altered trachyte consisting of feldspar microlites, fine grained with strong flow alignment. The second type indicates a higher degree of hydrothermal alteration.

4. Mau Tuff
   It is the oldest rock in the western escarpment of Olkaria area. Aged at Pliocene, the rocks are dominated by tuffs (welded and un-welded), minor rhyolites, trachytes and basalts. Mau tuff occurs around the Olkaria West Field close to well OW-304D overlain by pyroclastic layer up to 5 m thick. The tuffs are reddish brown, and mostly altered to greenish clay along facture planes. The Mau tuff acts as primary reservoir in Olkaria West Field.
5. Pre-Mau volcanics complex
   The unit conformably underlay the Mau tuff. It consists of phonolites, basalt, trachytes and tuff.
6. Proterozoic metamorphic gneisses and schists
   This basement rocks does not outcrop on the surface but is age at 590Ma (Pan African age).

According to Omenda (1998) the structural pattern in OGF mainly consists of four normal faults trending N-S, NW-SE, NNW-SSE and ENE-WSW. Faults and fractures are prominent pathway of heat transfer of geothermal system in OGF.

The N-S fault represents the latest tectonic activities of the rift floor. The occurrence of fumaroles activities is coincidence with some of N-S fault trends as a result of vertical permeability as can be observed along Ololbutot fracture zone.

The NW-SE trending faults associated with the alignment of volcanic centres are presented by the Suswa fault. These faults cut through the Trachyte Plateau. Therefore, they are older in comparison to other fault directions. The NNW-SSE high angle faults are represented by Mau escarpment in the western part of Olkaria.

The ENE-WSW trends are represented by the Olkaria fault crosses the geothermal area and is interpreted as rejuvenated structure about 50-100 m wide on the northern slopes of Olkaria Hill. It is associated with the fumaroles (occurring at boiling point), ground alterations, sulfur accumulations and intense silicification. The local surface displacement of Olkaria Fault is 5 meter vertical down throw to the north.

2.3.2. Geophysical and reservoir P&T observation

Resistivity observation (Muchemi, 1999) cited in (Dimitrios, 1989; Furgerson, 1972; Mwangi, 1986; Onacha, 1989) indicated that geothermal sources are observed as low resistivity associated with linear structures in NE-SW and NE-SE directions. In addition, interpretation of gravity data (Muchemi, 1999) cited in (Ndobi, 1981) showed that the body of source for geothermal source is located in the southern part of Olkaria which coincide with Olnjorowa gorge and Mt. Suswa alignment within W-E direction from Olkaria-Dome-Longonot .

High reservoir temperature distribution spreads along Olkaria East Field, Olkaria West Field and Olkaria Dome. The reservoir temperature range is recorded between 250°C to about 300°C (Ouma, 2005). Spatially, it is associated with faults from those trending in NNE-SSW, NE-SW and NW-SE directions. Similar association is also found in high geothermal pressure which is evident (e.g, along the Olkaria fault zones and Dome field in the Northeast and East Olkaria. However, the geothermal pressure shows decreasing trend (Muchemi, 1999).

Olkaria Geothermal Field is considered as shallow magmatic origin (Muchemi, 1999). The hot source is related to the continental rift system associated with sets of normal faults. The faults act as a hot source pathway and heat the water to produce the hot steam (figure 2.5). According to seismic and gravity studies, the heat source depth is around 4-5 km (Simiyu & Keller, 2000, 2001).

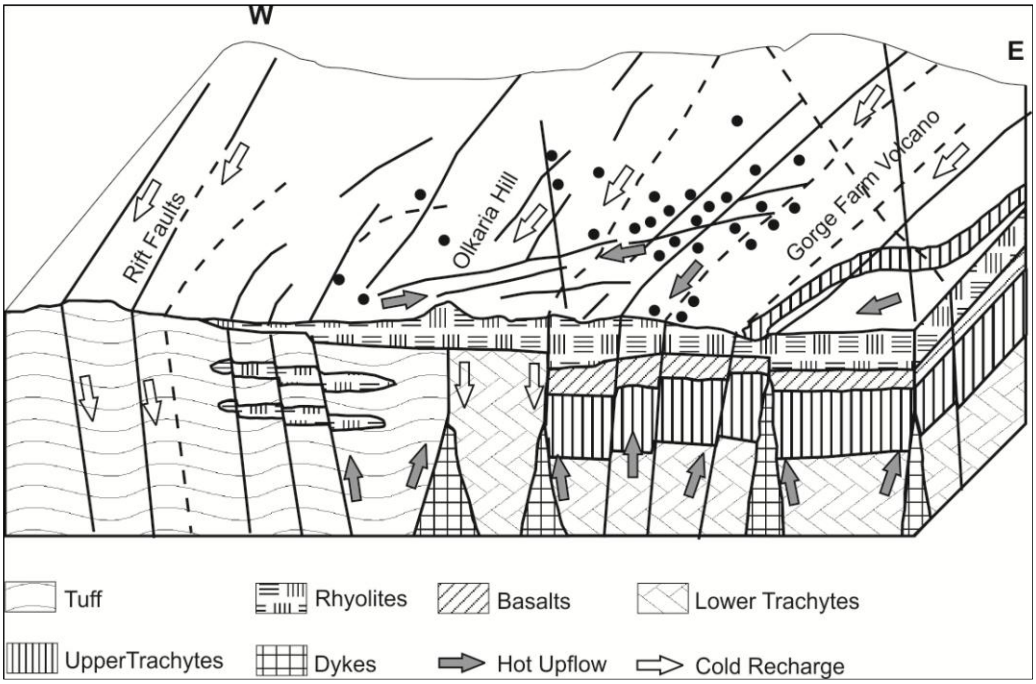

Figure 2.5: 3D conceptual model of Olkaria Geothermal Field, the black dots represent micro earthquakes distribution from seismic studies within the field (modified from Muchemi, 1999)

2.3.3. Production history and monitoring

Since its feasibility studies and exploration program finished at around 1977, the OGF started to begin its drilling production program in 1980s and the first power plant Olkaria East Field (Olkaria I) commenced producing about 45 MWe between 1981-1985 (Ouma, 2005). At present, there are at least seven fields being utilized for drilling production covering approximately 80km^2 (figure 2.6); Olkaria East (Olkaria I), Olkaria North East (Olkaria II), Olkaria Central, Olkaria South East, Olkaria North West (Oserian power plant), Olkaria West (Olkaria III) and Olkaria Domes.

Olkaria East Field (Olkaria I) is the most productive wells and its production has been monitored since first exploitation 1981 (figure2.7). In the Olkaria East Field (Olkaria I) 33 wells were drilled out of which 31 have been connected to the stream gathering pipes. Current status, however, shows that 25 wells are in productive status while the six wells are become non-commercial producer due to declining production over time (Ouma, 2005). From the six wells, the two wells are being used as reinjection wells (OW-3 and OW-6). The installed injection wells have significantly increases the life time of production wells from drying-up.

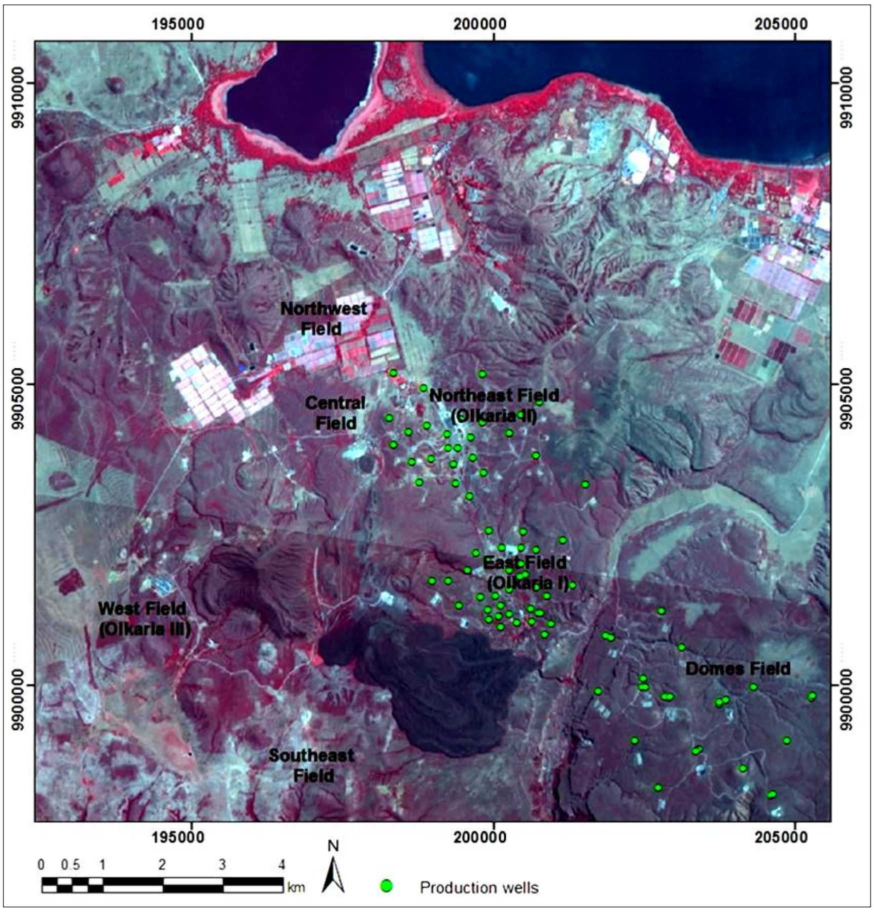

Figure 2.6: The Great Olkaria Geothermal Field covering the area of approximately 80 km². The green dots represent the location of production wells. Image overlying is ASTER RGB combination band 321 (Modified from Ouma, 2009, wells data from KenGen, 2011).

The monitoring of production wells has been conducted by the Kenya Electricity Generating Company Ltd (KenGen) from 1985 to up to now. It is reported every half year (first round is on July and second round is on November). For this study, we use production record up to second half of 2007 (Mburu, 2007). Figure 2.7 shows the average steam production history of Olkaria Geothermal Field until second half of 2007 production. The unit of steam production is in tonnage/hour or can be written as (t/hr). An increasing production was shown in the first three years of production (1981-1983). However, the declining trends occurred in the following years (around 1984 to 1994). Up to 2002, the trend had been increasing and continued to decline in the period of 2003 to 2007. Due to the declining trend over the following years of production, therefore, the company installed injection wells (mentioned above) to increase the production and prevent from reservoir drying (Ouma, 2005).

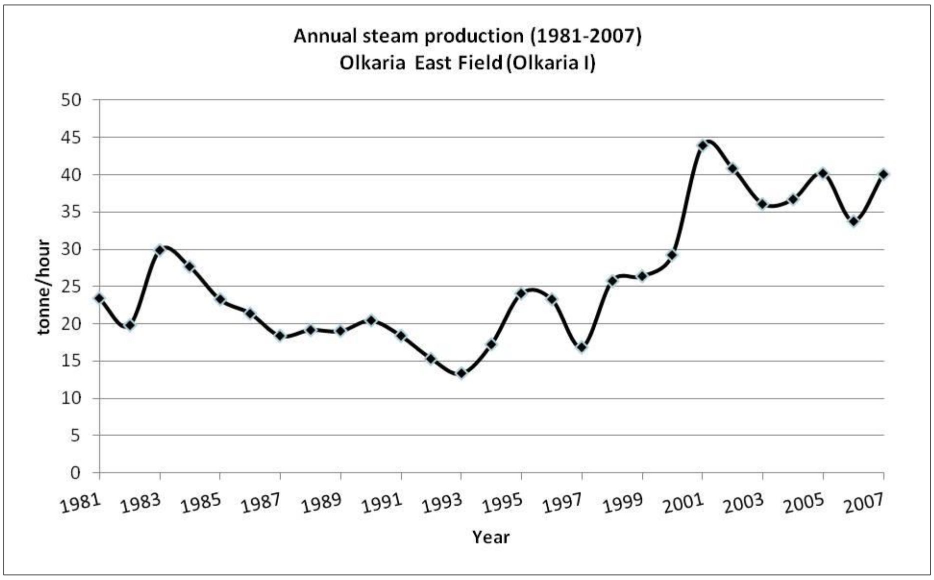

Figure 2.7: The annual production of Olkaria East Field (Olkaria-I), Olkaria Geothermal Field, Naivasha,Kenya.(modified from, (Mburu, 2007).

2.4. Groundwater extraction in Lake Naivasha and sourrounding

Exceed of groundwater extraction around Lake Naivasha and surrounding areas are potential cause for expected deformation in the study area. Becht & Nyaoro (2005) reported that the groundwater level in the north of Lake Naivasha showed decreasing trend as a result of large abstraction for irrigation purposes and domestic drinking water supply. The ground measurement of groundwater level around Lake Naivasha has been conducted in 1999 (Kibona, 2000), 2001 (Nabide, 2002) and 2004 (Yihdego, 2005). The decreasing trends over 3 meters occurred from the first observation in 1999 until 2004 in the north of Lake Naivasha.

2.5. Previous works on regional deformation studies in KRV

2.5.1. Geophysical studies

The geophysical studies of the Kenya rift valley are known from the work of several methods such as gravity studies (Maguire et al., 1994) and seismic refraction-wide-angle reflection experiments (Mechie et al., 1994) which undertaken to reveal the lithosphere structure of the rift system.

The geophysical studies was done by Keller (1994) suggested that the crustal thickness beneath the rift floor is about 30 km at latitude 0.5°, 40 km and 35 km thick in western and eastern flank respectively. The crust as such is thickening as more outward from the rift zones. Its rift asymmetry might be due to the tilted blocks of normal faulting associated with listric and roll-over structures.

In addition, the rift floor is covered by sediment and volcanic layer approximately 2600 m thick in the west margin and 2000 m thick in the east margin (Olivier, 2011), as inferred from regional negative Bouguer anomaly. This evidence also support the uplift occurs in asthenospheric body which cause the lithospheric thinning indicated by decrease in mantle velocity to the depth of 150 km. The negative anomaly also interpreted as dyke injection occurred in the middle of the grabens as related to the magma reservoir (Simiyu & Keller, 2001). Similar finding also done by Olivier (2011) confirmed that both west and east arms plateau of East African Rift have negative regional Bouguer anomalies. Considering its process, the East African Rift can be categorized as plume-related rift.

2.5.2. Micro-earthquakes

Seismic activities in Africa are mainly concentrated in East African Rift reflected by earthquake pattern distribution along the continental margin. The investigated earthquake seismicity is a mix between oceanic and continental source with the maximum depth of the epicentre being 40 km (Chorowicz, 2005).

Seismic activities along the East African Rift have been reported by several researchers (Maguire et al., 1988; Tongue et al., 1992). Seismic activities observed in Cenozoic Kenya rift valley showed magnitude < 3 in western branch and magnitude > 4 in eastern branch, thus indicating higher energy released in eastern rift. Further, recent volcanism, geothermal activities, shallowing litho-asthenosphere boundary and regional structural features seems associated with seismic activities within the rift system.

The regional network of seismic observation within the Kenya rift valley for periods between 1993-1996 (Hollnack & Stangl, 1998) reveal approximately 2000 micro-earthquakes records including 435 points which had magnitude >5. The areas with highest seismic activities recorded were in the central Kenya rift valley (Nakuru), Northern Tanzania, North-Eastern Kilimanjaro and Nyanza Rift (western Kenya).

The earthquake magnitude > 5 is potential for surface deformation. Therefore, the record of the paleo-seismic during Quaternary time (< 2 million years ago) is necessary for seismically hazard assessment (Walling & Mohanty, 2009).

Figure 2.8 shows active seismicity of East African Rift System (EARS) based on regional and local seismicity observed along the rift system.

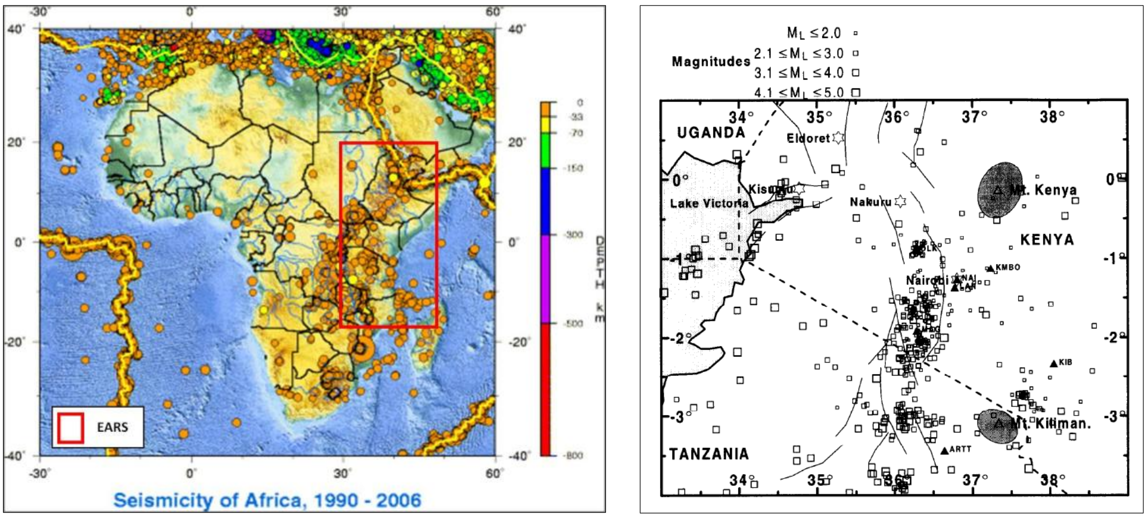

Figure 2.8: Regional seismicity map of Africa observed 1990-2006 (source: USGS) (left). Local seismicity map of Kenya observed 1993-1996 (source: University of Nairobi, 1997) (right).

2.5.3. Neotectonic of the East Africa Rift System (EARS)

Neotectonic is the tectonic activities related to the earth surface deformation from late Miocene (Neogen) to Quaternary age (about 10,000 years ago to recent) which can be captured by recent topographical features. It is close related with active faults which can be traced regionally by remote sensing image interpretation and seismicity observation (Skobelev et al., 2004).

The series of active faults along the EARS is associated with active seismic zones with less than 5 MMI (Strecker, et al., 1990). Delvaux & Barth (2010) interpreted active faults regionally using DEM SRTM 90 m. According to their study, active faults were associated with recent volcanism, geothermal activities and hot spring. Similar conclusion is drawn from the work of Becht & Harper (2010) and Kuria, et al. (2010)

analysed the active faults from higher resolution remote sensing imageries (ASTER 30m) together with sub-surface geophysical data and detail field geological mapping.

Neotectonic studies can be applied as first sight indicator of the potential geothermal occurrence. The related activities such as active faults mechanism, hot springs, recent volcanoes are the main signatures of the surface recognition which insight to geothermal prospects.

Strecker, et al. (1990) reviewed the neotectonic evolution along the EARS segments in relation with morphology, lithology, surface structure, fault mechanism and volcanism. Changes on rotational extensional forces triggered the rifting system in central Kenya rift. The most recent rift system has rotated from east-west direction into slightly northwest-southeast extensional forces. This study is based on the interpretation of the main faults regionally related to the tectono-stratigraphy (Figure 2.9).

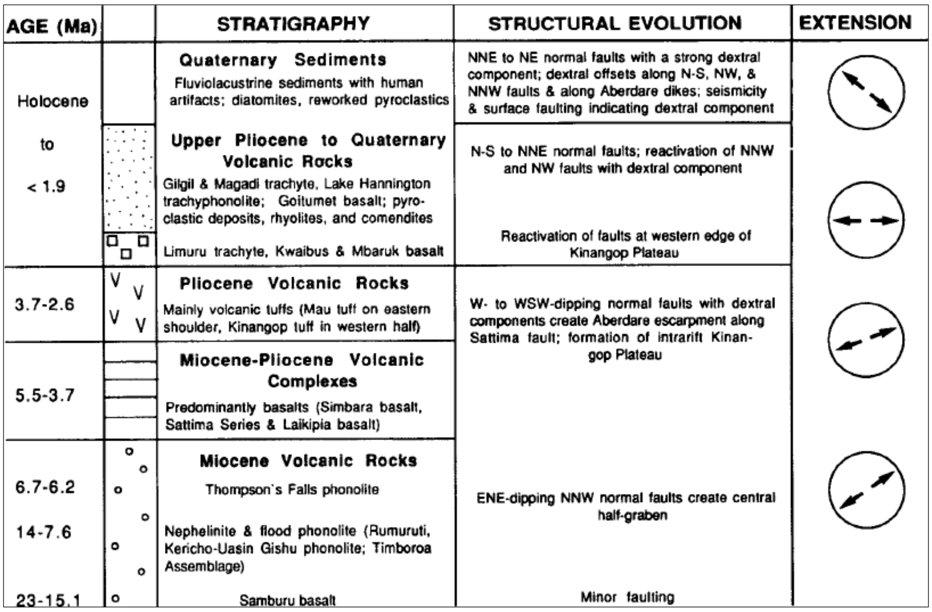

Figure 2.9 : Tectono-stratigraphic diagram of central Kenya rift (Strecker, et al., 1990).

2.5.4. InSAR for deformation studies in KRV

InSAR application for deformation related to the tectonic activities within the KRV has been applied by several researchers (Biggs J. et al., 2009; Kuria, 2011). Kuria (2011), applied differential interferogram (DinSAR) to map the single deformation induced by small earthquake in Lake Magadi, southern part of Kenya Rift Valley. The small cm scale of displacement along the line of sight (LOS) radar satellite has been revealed from 4-pass differential interferometry in relation with the local seismic event in 2005. This study is very significant for the seismotectonic study over the area. In addition, similar work using multiple DinSAR was carried out by Biggs et al. (2009) in order to monitor the deformation induced by active volcanoes along the Kenya Rift Valley. This geodetic volcano monitoring has been revealed the subsidence and uplift related to the multiple deflation and inflation volcanoes along the Kenya Rift Valley; e.g. 2-5 cm deflation in Mt.Suswa and Mt. Menengai (1997-2000), approximately 9 cm inflation deformation occurred in Mt. Longonot (2004-2006) and nearly 21 cm inflation deformation occurred in Mt. Paka (2006-2007). The source model fitting deducted from DinSAR deformation episode showed the depth of 2 – 5 km corresponding to the active magmatic system source beneath these volcanoes.

3. DATASET AND METHODOLOGY

This chapter describes the dataset and methods used to reach the research objectives. A major part of the research is geared towards InSAR processing to map the surface deformation while the other methods are used to support the InSAR result. General flow chart of whole research and data compilation were also displayed with the detail explanation of each step.

3.1. Dataset

The dataset for this study is divided into two parts comprising of primary data and secondary data.

3.1.1. Primary data

The primary dataset comprise of active and passive remotely sensed data (see Table 2). These were used for the interpretation of geological and structural features including land use patterns. The remotely sensed datasets were also used in fieldwork planning and verification of interpreted results. In this study, all datasets (remotely sensed images and other vector layer) products were projected into WGS 84 UTM zone 37 S.

Table 2: Description of primary dataset used for this research

No	Data	Level Data	Format data	Resolution	Specification
1	ASTER VNIR	level 1b	Raster	15 m	Band 1-3 (0.52 – 0.86 µm), cover 60 km x 60 km
2	6 Envisat ASAR Single Look Complex (descending mode): 1. ASA_IMS_1PNUPA-20031027 2. ASA_IMS_1PNUPA-20031201 3. ASA_IMS_1PNUPA-20060703 4. ASA_IMS_1PNUPA-20060807 5. ASA_IMS_1PNDPA-20070305 6. ASA_IMS_1PNDPA-20080218	level 1b	Raster		Microwave radar C-band, VV(single polarization), high resolution slant range mode, consist phase and intensity, cover 100 km x 100 km
3	Digital Elevation Model (DEM) SRTM		Raster	90 m	Elevation data generate from radar technology
4	Field observation		Point		

3.1.2. Secondary data

The secondary datasets were acquired from the third party organizations which are listed in Table 3.

Table 3 : Description of secondary dataset used for this research

No	Data	Format data	Source
1	Regional geology map of Naivasha	Vector	ITC (Naivasha research group)
2	Base map (road, drainage, cities)	Vector	ITC (Naivasha research group)
3	Groundwater levels measurement	Table (X,Y)	ITC (Naivasha research group)
4	The location of geothermal and reinjection wells	Vector	KenGen Ltd.
5	The production from 1985 to 2007	Table &report	KenGen Ltd.

3.2. Software used

Table 4 shows software used during this study.

Table 4: Description of the software used for this study

No.	Purpose	Software
1	Image processing	ENVI 4.8 ILWIS 3.3 Academic version
2	Radar Interferometry generation	SARscape 4.3
3	GIS and data integration	ArcGIS 10.0
4	Thesis writing, tables, slides and graphics	MS Office Corel Draw X5

3.3. Methods

Figure 3.1 shows the general flow-chart of the current study

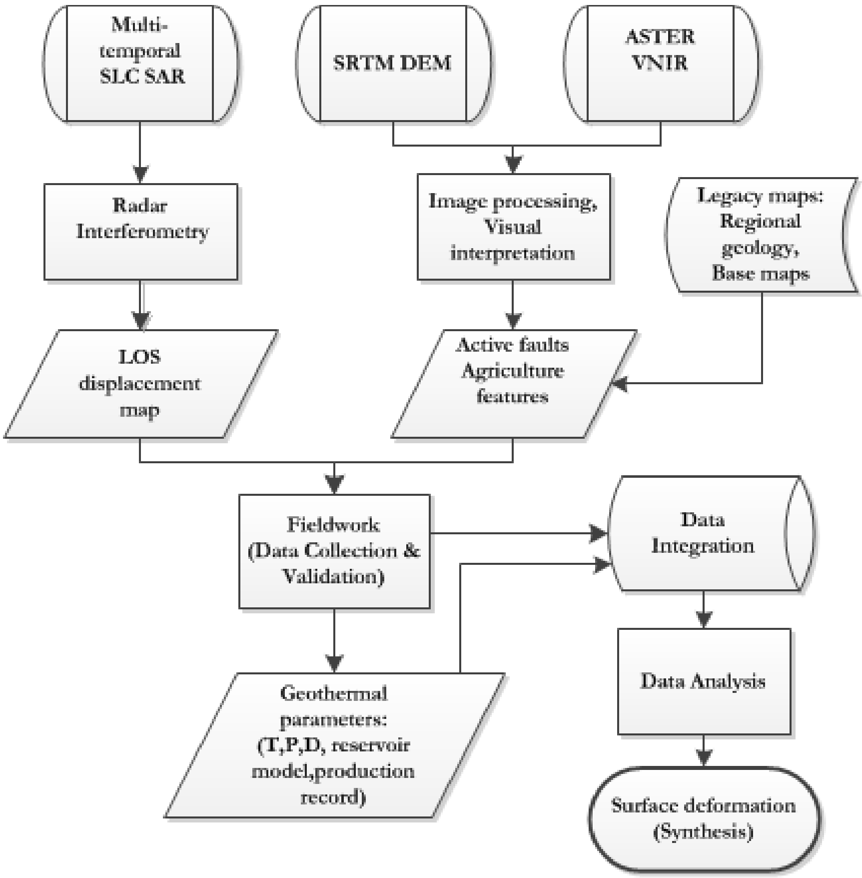

Figure 3.1: The general flow chart of the applied methodology

3.3.1. Multi-temporal InSAR processing

InSAR is a method using two SAR images, acquired by two different SAR antennas or single antenna in two different acquisition time. The phase difference between the two images is calculated to measure the height (Hoen & Zebker, 2000). InSAR has developed from a theoretical concept into an application in a wide range of earth science related problems. Currently, the application of InSAR is widely used in creating digital elevation of Earth surface and also in deformation studies. The geometry of InSAR is illustrated in figure 3.2.

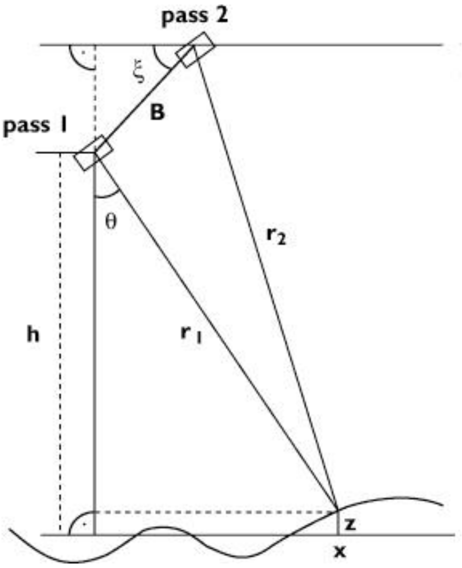

Figure 3.2: The simplified geometry of radar interferometry taken from two repeat pass radar (pass1&2), z is represented of ground elevation measured by repeat pass radar sensors (European Space Agency, 2011)

As illustrated in Equation 1, the phase difference φ taken from the repeat-pass radar sensor (pass1 & pass 2), is the function of the baseline (B), satellite incident angle (θ), satellite radar wavelength (λ) and the satellite height (h). It can be explained mathematically as:

$$\varphi = -\frac{4\pi}{\lambda}(|r_2| - |r_1|) \qquad \text{Equation 1}$$

Phase difference received from the two SAR sensors consists of at least five contributing factors according to the equation as follow (Hanssen, 2001) :

$$\varphi = \varphi top + \varphi disp + \varphi ref + \varphi atm + \varphi noise \qquad \text{Equation 2}$$

Where:

φ : Interferometric phase different.
φtop : Phase contribution from the topographical signatures.
φdisp : Phase contribution from the earth surface displacement.
φref : Phase contribution due to orbital inaccuracy.
φatm : Phase contribution due to phase delay due to atmospheric water vapour.
φnoise : Phase contribution due to error on radar instrumentation.

Some relevant terms of InSAR and technical description were used during the InSAR processing and interpretation. Each term were described as follow:

1. Baseline
   Baseline is the geometry of the separation of two repeating satellite orbits or two antenna positions in radar airborne.
2. Coregistration
   Coregistration is a resampling of SLC slave image into SLC master image at sub-pixel accuracy level. This pixel alignment should not be less than 0.2 pixel of pixel matching in order to reduce the interferometric correlation (Zhengxiao & Bethel, 2008).

3. Multilooking
   Multilooking is the method to convert SLC images into intensity (amplitude) image after phase separation. The number of look is applied at 5 pixels for azimuth direction and 1 pixel for range direction to achieve approximately squared pixel at ground range resolution.
4. Interferogram
   Interferogram is the process of complex multiplication of two coregistered images (master and slave) to extract the phase difference between them.
5. Coherence
   Coherence is defined as a degree of similarity of coregistered pixel taken from the two SLC images (Hanssen, 2001), in this case, master and slave images. Coherence statistically ranges from 0 (no correlation) to 1 (full correlation). The coherence generation also is utilized to assess the quality of interferogram.
6. Interferogram fringe
   Interferogram fringe is the visualization of the phase value in the interferogram range from 0 to 2 π in a full colour cycle
7. Phase Unwrapping
   Unwrapping interferogram is very important during InSAR processing. The sufficient method need to be undertaken to minimize error during interpolation e.g sudden phase jumping or phase discontinuity (Hanssen, 2001).
8. LOS (Line of Sight)
   Line of sight can be defined as a slant range direction. It is the angle of radar platform/antenna with the horizontal plane during transmitting and receiving signal from the object on the ground which is calculated from the north.

In this study, two methods of surface deformation map using InSAR approach were utilized, namely, two-pass Differential Interferogram (DinSAR) and interferogram stacking using small baseline subset (SBAS).

1. Two-pass differential Interferogram (DinSAR)

The following description is the steps were acquired during two-pass differential interferogram (DinSAR) generation:

- **Import and Focusing**

  Available Envisat ASAR datasets were imported to generate Single Look Complex (SLC) that can be read by the software. It comprises of phase and intensity (amplitude) preserved in each pixel of slant range. At this stage, DORIS file, was also added into SLC image. DORIS file is the precise orbital parameters for ENVISAT. It consists of the information about latitude, longitude, height and height rate. Thus, the corrected orbital SLC image was produced which can be used as master and slave images for interferogram generation.
- **Baseline Estimation**

  This step is an optional. In this study, it was used to assess the suitability of image pairs for interferogram generation. The perpendicular baseline between slave image (pass 1, Figure 3.2) and master images (pass 2 in Figure 3.2) was preferably set to less than 300 m in order to minimize the phase shifting during the interferogram generation.
- **Interferogram Generation**

  After selecting the sufficient baseline, the interferogram was generated by estimating the phase difference (see Equation 3.1) between master and slave images. The output is a raw interferogram comprises of all phase signatures; e.g, topography; earth surface displacement; atmospheric delay, orbital inaccuracy and also noise from radar instrumentation. The interferogram comprises of phase numbers, each phase cycle equal to 2π, and it was displayed as a contour like image. The coregistered and multilooking of two SLC images were also generated at this stage.

- **Interferogram Flattening**
  The previous interferogram was flattened using DEM SRTM 90 m resolution. In this process, residual/differential phase was separated from two phase contributions; 1) constant phase due to InSAR geometry system and 2) known topographic phase. Thus, the differential phase that was extracted was assumed to be associated with earth surface displacement phase.
- **Filtering and coherence generation**
  Noise and other error contributing to differential interferogram were reduced by filtering process. In this study, Goldstein filter (Goldstein & Werner, 1998) was used to enhance the strong signal related to high amplitude of interferogram. Conversely, the lower amplitude which assumed related to noise will be suppressed (Hanssen, 2001). Along this step, a coherence map was generated.
- **Phase unwrapping**
  The filtered interferogram was unwrapped using the minimum cost flow algorithm (Costantini, 1998) to obtain absolute phase values and to dissolve 2π phase ambiguity from the previous wrapped interferogram (differential interferogram).
- **Obital refinement and re-flattening**
  During orbital refinement, 25 ground control points were collected from filtered interferogram image. These points were spread out the whole scene of the image. The areas of high coherence were prioritized to place these points. The unwrapped interferogram was refined and re-flattened to minimize the unwanted phase due to topographic artefacts, noise, and atmospheric disturbance.
- **Phase to displacement and geo-coding**
  The unwrapped interferogram was converted into surface displacement map according to the Line of Sight (LOS) direction. The grid size is set to 30 meter resolution and bilinear method was used for pixel interpolation.

2. Stacking Interferogram using small baseline subset (SBAS)

The interferogram stacking method using small baseline subset (SBAS) was applied in this study. SBAS is the advance technique on DinSAR which aims to reduce the spatial (baseline) and temporal (time acquisition) de-correlation by combining an appropriate differential interferogram pairs which characterized by small orbital separation (baseline) (Berardino et al., 2002).

The following steps were required for stacking interferogram:

- **Connection graph**
  In this step, all possible interferogram pairs of SAR dataset were subset according to the small baseline threshold. The interferogram combination were selected based on the singular value decomposition (SVD) method (Berardino, et al., 2002).
- **Area of interest definition**
  In this step, the SLC images were subset to the study area. This step was required to reduce the long computation resources.
- **Interferogram generation**
  Differential interferogram was generated in this step. The unwrapped differential interferogram pairs were processed using two steps processing procedure extending the spars-grid approach (Costantini & Rosen, 1999). Moreover, atmospheric phase signals was filtered in space-time deformation following the same procedure such as in Persistent Scattered interferogram (Ferretti et al., 2001).
- **SBAS inversion**
  Finally, deformation velocity estimation was calculated based on the simple inversion of a linear model.

Ideally, SBAS method is applied in large number of SAR image acquisition to increase the temporal sampling. However, considering the dataset is high temporal baseline, this method is utilized in this study.

3.3.2. Interpretation of active fault

Regional active faults and lineament were interpreted from hills-shaded SRTM 90m. To create the shaded relief, an inclination of 45° sun angle and the three-directional illumination angles (270 W, 315 NW, 0 N) were applied on the SRTM DEM. This method is sufficient to sharpen the topographical expression related to surface faults alignment (Delvaux & Barth, 2010).

Vector file representing fault segments were digitized during visual image interpretation. The local structural lineaments from the Olkaria Geothermal Field were also added to the new interpreted map to obtain more understanding of the active faults over the study area.

3.3.3. Extracting the agriculture areas from ASTER image

Image processing of ASTER in VNIR range (0.52µm – 0.86µm) were done to create the RGB false colour composite (FCC) in band combination 321. Visual interpretation elements of identification of agriculture areas was carried out based on its pattern, shape and tone (Drury, 2001). This information aids to validate the surface deformation due to groundwater extraction within agriculture activities in the study area.

3.3.4. Fieldwork

Three weeks fieldwork campaign was carried out from 13th September 2011 to 3rd October 2011 aimed to validate the surface deformation map generated by InSAR supported by surface structure interpretation from DEM SRTM image. About 55 points of field observation were collected and recorded using GPS covering the study area. The field observations are mainly concentrated in the Olkaria Geothermal Field and faults dissected areas along the rift margin.

These points were saved as primary data (Table2) and constructed in the format database comprises of data attributes; e.g. coordinate location (X,Y), station number, structural measurements (dip, fault trends), lithology, land cover and morphology observation, hot spring, and field photo collection (Appendix:1).

In addition, collecting secondary dataset from Kenya Electricity Generating Company Ltd. (KenGen), the Geothermal Company operating in Olkaria Geothermal Field, were also done to obtain geothermal parameter dataset such as: production record, temperature, pressure, depth, reservoir boundaries and reservoir model.

During fieldwork campaign, the groundwater level measurement was supposed to be conducted with the WARMA (Water Authority Management), a government institution on groundwater management, and linked it with the previous measurement. However, it was not successful due to technical problem on equipment and resource issues.

3.3.5. Data integration and analysis

All processed remotely sensed dataset and supporting datasets were integrated to interpret the cause of surface deformation within the study area. The data integration part is treated in Chapter 5.

4. RESULTS

This chapter describes the results obtained from: 1). Surface deformation map in Line of sight (LOS) direction using InSAR 2). Surface active fault interpretation from DEM SRTM including its fieldwork validation and 3). Extracting the agriculture features from the ASTER image.

4.1. Surface deformation from InSAR

4.1.1. Two-pass differential interferogram (DinSAR)

From the fourteen possible interferogram pairs, six pairs were selected according perpendicular baseline criterion discussed above. Table 5 shows the specifications regarding the interferogram pairs used, with code (M) representing the master image, and (S) the slave image including the temporal baseline information, doppler difference, and geometric parameters for each SLC images.

Table 5: Envisat ASAR Interferogram pairs for InSAR generation

No	Interferometric pairs	Temporal baseline (day)	⊥ Baseline (meter)	Doppler Diff.	Orbit	Track
1	2003/10/27 (M)	35	246	-456	8663	92
	2003/12/01 (S)				9164	92
2	2003/10/27 (M)	1225	168	-456	8663	92
	2007/03/05 (S)				26198	92
3	2003/10/27 (M)	1575	123	-456	8663	92
	2008/02/18 (S)				31208	92
4	2003/12/01 (M)	1190	78	-456	9164	92
	2007/03/05 (S)				26198	92
5	2006/07/03 (M)	35	42	-456	22691	92
	2006/08/07 (S)				23192	92
6	2007/03/05 (M)	350	291	-456	26198	92
	2008/02/18 (S)				31208	92

Figure 4.1 comprises of three significant areas where some low rate surface deformation is expected within five year monitoring (2003-2008). These include: 1) The Geothermal site of Olkaria, where continuous extraction of geothermal fluid is undergoing, 2) Mechanized agricultural field where extraction of groundwater is very prominent, and 3) Active faults and volcanoes (Mt.Longonot in the south), where it is expected to display earth surface deformation as the area is slightly associated with seismic event and continuous volcanic activities.

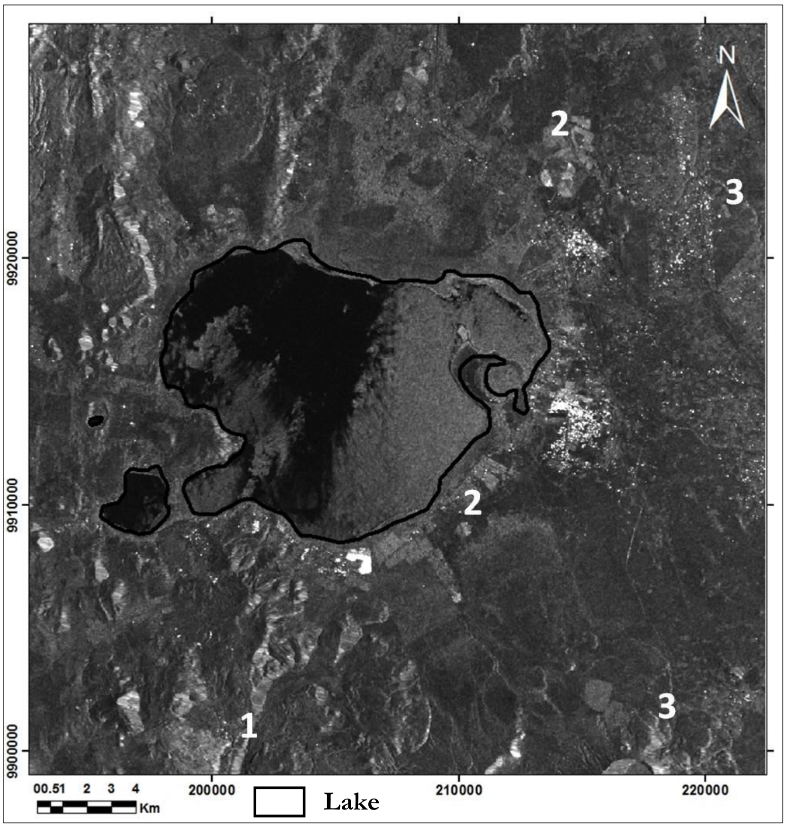

Figure 4.1: Geocoded Envisat intensity image covering the area of interest for possible surface deformation:
1). Olkaria Geothermal Field 2). Groundwater extraction in agriculture areas and
3).Active faults segments and active volcano

The six ENVISAT images, from 2003 to 2008 (with two years 2004 and 2005 missing), were required in slant range for visual data inspection. As a result, the multilooking to the ground range resolution was first performed on the six SLC images subset according to the area of interest.

Figure 4.2 displays the six intensity images that are useful to approximate land cover variety changes during multitemporal radar image acquisition in the area of interest. By visual inspection, the urban areas, locates in the eastern part of the lake, shows high intensity backscattered signal and relatively unchanged during five years observation, while the other areas indicates the variation in degree of backscattering signal. The high intensity backscattered signal reflects high phase values which are significant for the interferogram generation.

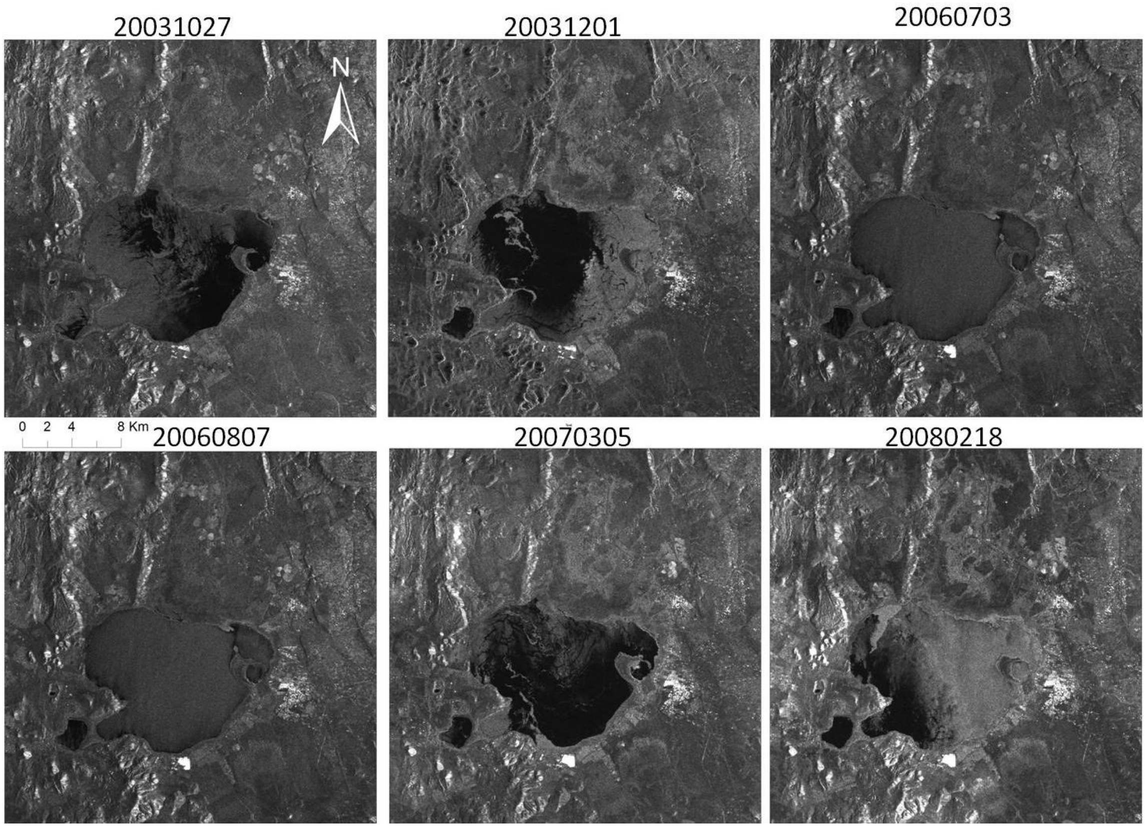

Figure 4.2 : Geocoded six intensity images within five years observation covering the area of interest

4.1.1.1. Coherence computation

The coherence image was attempted to assess the quality of interferogram. Figure 4.3a displays the coherence images that were subset into the area of interest. Spatially, the high coherence (indicated by scale of 1 in white colour) occurred in the pairs of small temporal baseline and the low coherence (indicate by scale 0, black areas) occurred in the pairs of longer temporal baseline. The low coherence also exposed in the Lake Naivasha (see the black polygon in figure 4.3a). This condition might occur due to the wave activity on the surface water thus creating diffused backscattered signal in different time during image acquisition.

In order to assess the coherence values, the area of Interest (AOI) for the specific areas, AOI 1 (geothermal field), AOI 2 (agriculture areas), and AOI 3 (volcano and active faults segments) (shown in colour polygon, in figure 4.3a) was created and the local statistics over the AOI were calculated over six pairs of coherence images. The average coherence was summarized in Table 6.

Table 6: The average of coherence derived from six SLC Image pairs

No	SLC Image pairs	AOI 1 (red polygon)	AOI 2 (yellow polygon)	AOI 3 (green polygon)
1	20031027-20031201	0.435	0.459	0.467
2	20031027-20070305	0.221	0.234	0.217
3	20031027-20080218	0.255	0.247	0.232
4	20031201-20070305	0.257	0.265	0.241
5	20060703-20060807	0.501	0.502	0.507
6	20070305-20080218	0.350	0.352	0.350

From Table 6, most of the coherence average among the area of interest (AOI) in six SLC images was considered low (less than 0.4) (Yonezawa & Takeuchi, 1997). Two pairs have the suitable coherence (average more than 0.4) that can be identified in the image pair of 20031027-20031201 and 20060703-20060807 respectively. One pair has the value slightly close to 0.4 shown in the image pair of 20070305-20080218.

The image pairs of 20031027-20031201 and 20060703-20060807 have a suitable coherence because the time span was short (35 days) and it is expected to show relatively fewer changes on the surface. In this case, the coherence might relate to the temporal variation. The longer the time acquisition the more changes is expected to occur. Such changes could be due to the vegetation covers, cultivating areas, constructions and also the atmospheric variation.

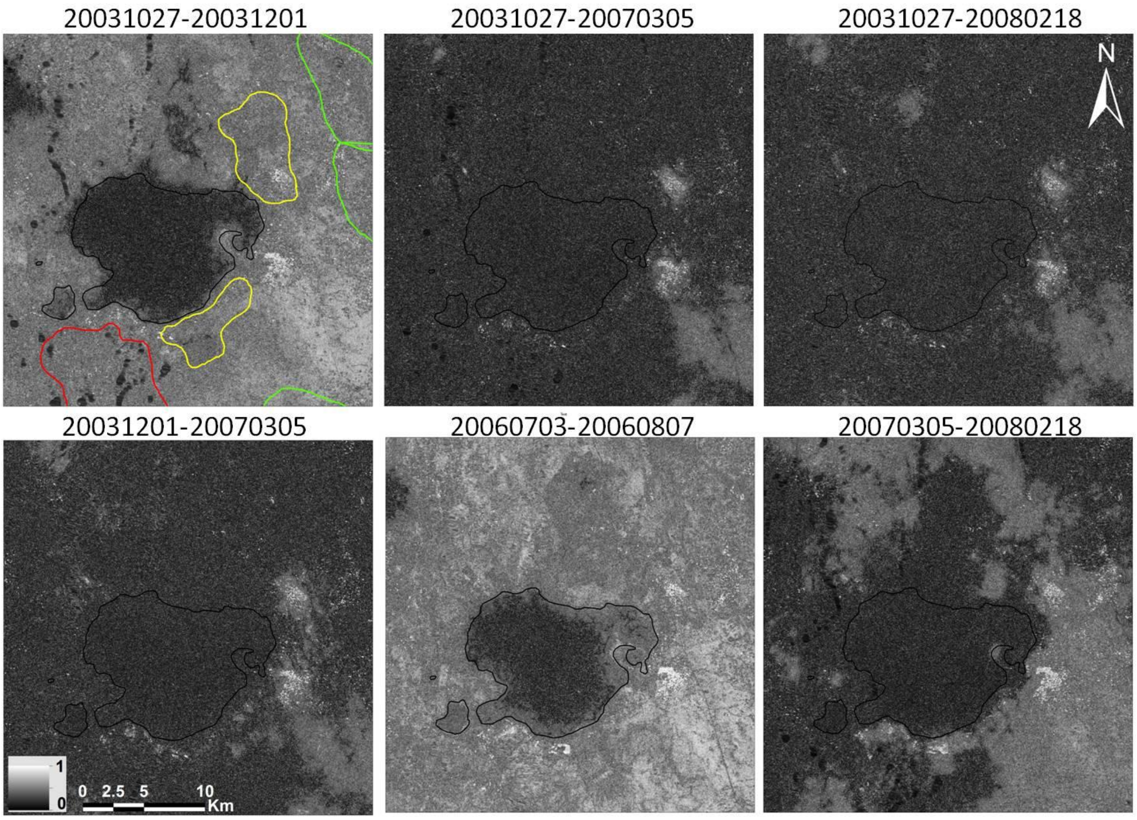

Figure 4.3a: Geocoded series of coherence image of six pairs; black polygon represent the Lake Naivasha, colour polygons represent the area of interest; red (geothermal area), yellow (agriculture areas), green (volcano and active fault segments)

4.1.1.2. Interferogram Generation

Figure 4.3b shows the differential wrapped interferogram represented by repeated colour fringe in a 2π cycle. Filtering has been applied to these images in order to suppress the noise. Thus, it enhances the quality of interferogram.

Most of the colour fringes develop in the areas with high coherence. Surface deformation activities can be seen slightly in the Southeast part of the study area associated with Mt. Longonot (Location D2) in the period of longer observation; e.g 20031027-20070305, 20031027-20080218 and 20031201-20070305 respectively. This might due to the inflation and deflation volcano activities triggered by shallow magmatic source.

The Olkaria Geothermal Field which is located in the Southwestern part of Lake Naivasha was dominated by noise over the longer temporal baseline interferogram. Although fringes are evident in the less vegetated small hill of Ololbutot Lava (Location D1), the full fringe and the scale were considerably small. Thus, it is difficult to interpret.

The agricultural activities along the Lake still show some fringes in the interferogram, although most are lost due to lack of coherence in the field. As could be measured during this period, InSAR application in cultivated areas suffer due to seasonal variation in image acquisition that lead also to poor coherence generation (Hanssen, 2001).

Whereas, in the period of short observation; e.g 20031027-20031201 and 20060703-20060807 the interferogram does not developed completely, and although the InSAR pairs have shown observation in the short period (35 days), no surface deformation such as sudden earthquake or big landslide or volcano eruption that might trigger the surface deformation could be measured during this period. In fact, there is no such event reported within this area.

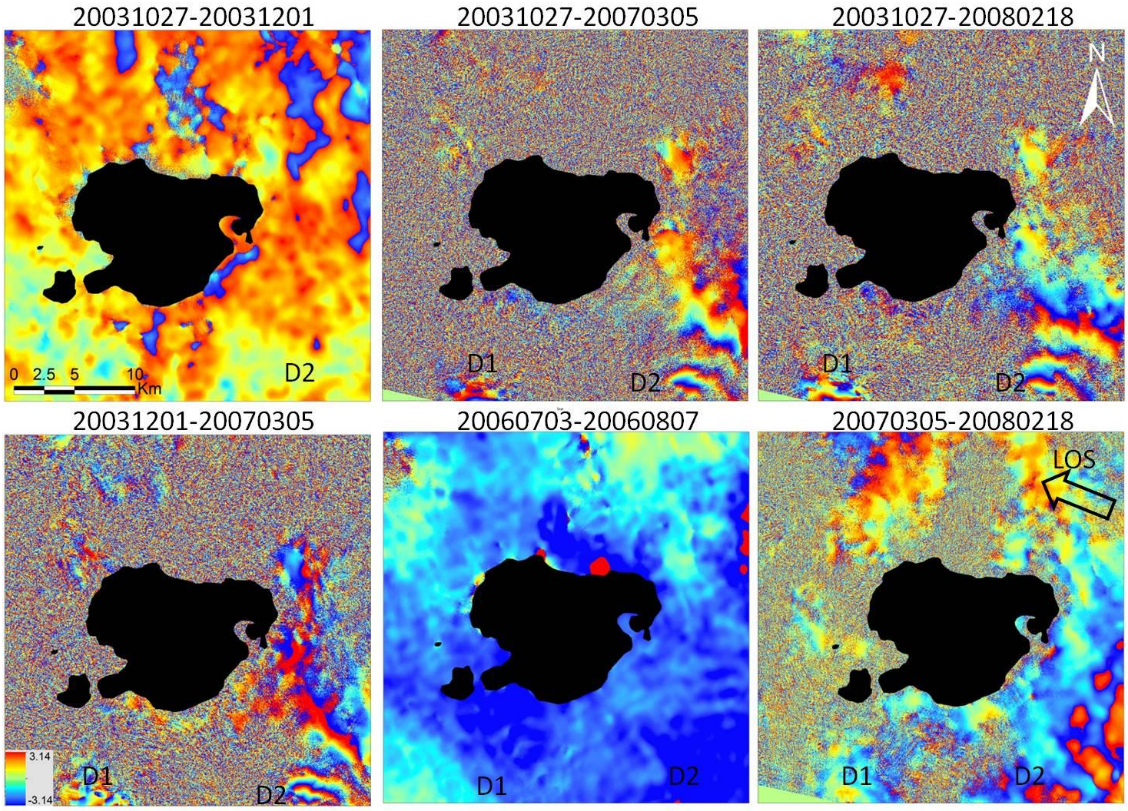

Figure 4.3b: Geocoded wrapped differential interferograms in five years image acquisition

4.1.1.3. Phase Unwrapping

During phase unwrapping, phase discontinuity occurred in the study area of steep topography. It is visible in the N-S hill, in the northern part of Lake Naivasha (see interferogram pair 20070305-20080218, Figure 4.4), where the area of blue (0.25 π) is seen to suddenly jump into the area of red (1.5 π).This feature need to be considered as insufficient information during interferogram interpretation.

Figure 4.4 shows absolute phase values represented by unwrapped interferogram that can be interpreted as surface displacement along the satellite line of sight (LOS). Images of unwrapped interferogram pairs were visualized in rainbow colour fringes. Each full cycle of colour fringes (blue-green-yellow-red) represent one phase (in scale of 2π or $-\pi$ to π). Since Envisat ASAR operates at C-band (5.6 cm), then 2π value is equal to 2.8 cm or 28 mm. The displacement values were counted according to the number of colour fringes cycle. If there were less than one fringe colour developed, the sliced colour fringes then can be (0, 0.5 π, π, 1.5 π) and multiplied by the 28 mm (2π).

According to the result of unwrapped phase in figure 4.4, overall colour fringes from six interferogram pairs do not show any full colour fringes cycle. However, one pair of interferogram in 20070305-20080218 shows some signal on deformation. This pair will be utilized in data integration part in order to analyze the surface deformation (see discuss in chapter 5).

Two-pass differential interferogram during five years observation (2003-2008), could not capture the low deformation in the area. Uncorrelated pixels (low coherence) and significant noise were dominant in the longer temporal baseline interferogram pairs. Those might contribute to the error during interpolation process to calculate the surface displacement along the line-of-sight (LOS) direction.

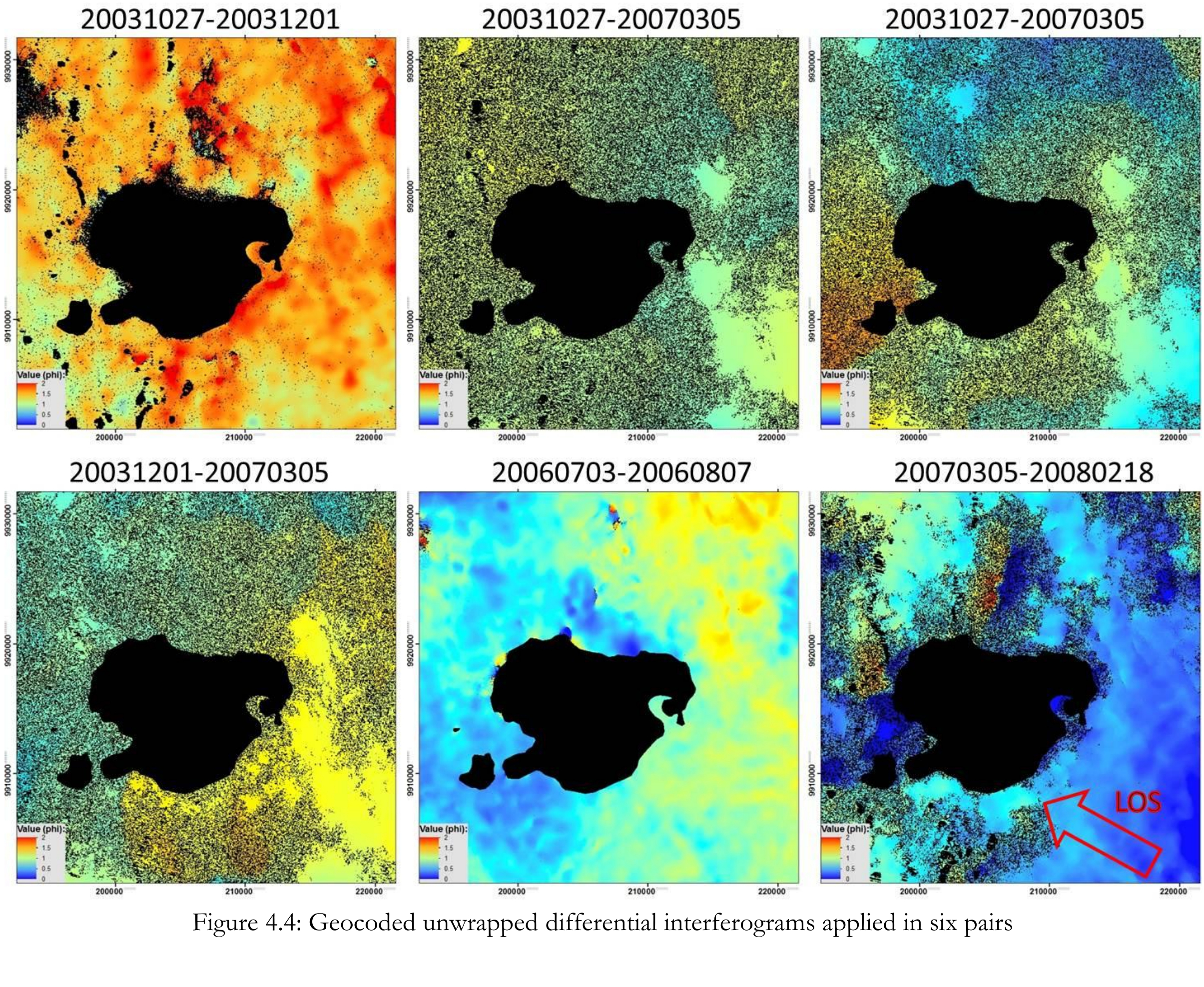

Figure 4.4: Geocoded unwrapped differential interferograms applied in six pairs

4.1.2. Stacking Interferogram using small baseline subset (SBAS)

In this study, the interferogram pairs were defined according to the mutual baseline threshold in range 30 to 300 meter. Any pairs outside this range will not be processed using SBAS algorithm (Figure 4.5).

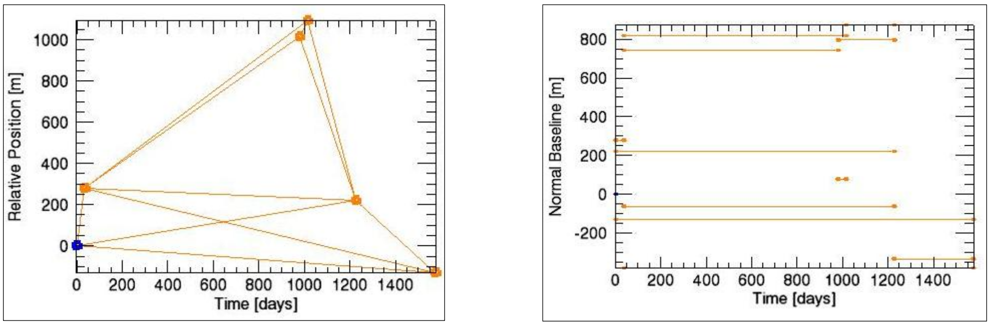

Figure 4.5: Combination of temporal baseline of six available slc images dataset with the set of normal baseline.

The six scenes of SLC images were subset to the study area and interferogram stacking generation was processed and coherence was averaged from whole pairs. The inversion linear model was then applied to compute the displacement rate in mm/year. Figure 4.6 displays the average of slow rate deformation occurred in the study area for five years observation from 2003 to 2008. The range of deformation rate is from -15 mm to 15 mm per year. The detailed interpretation of the surface deformation occurred in the area of interest will be discussed in the chapter 5 (data integration and result), to obtain the complete features after integrating with other supported dataset.

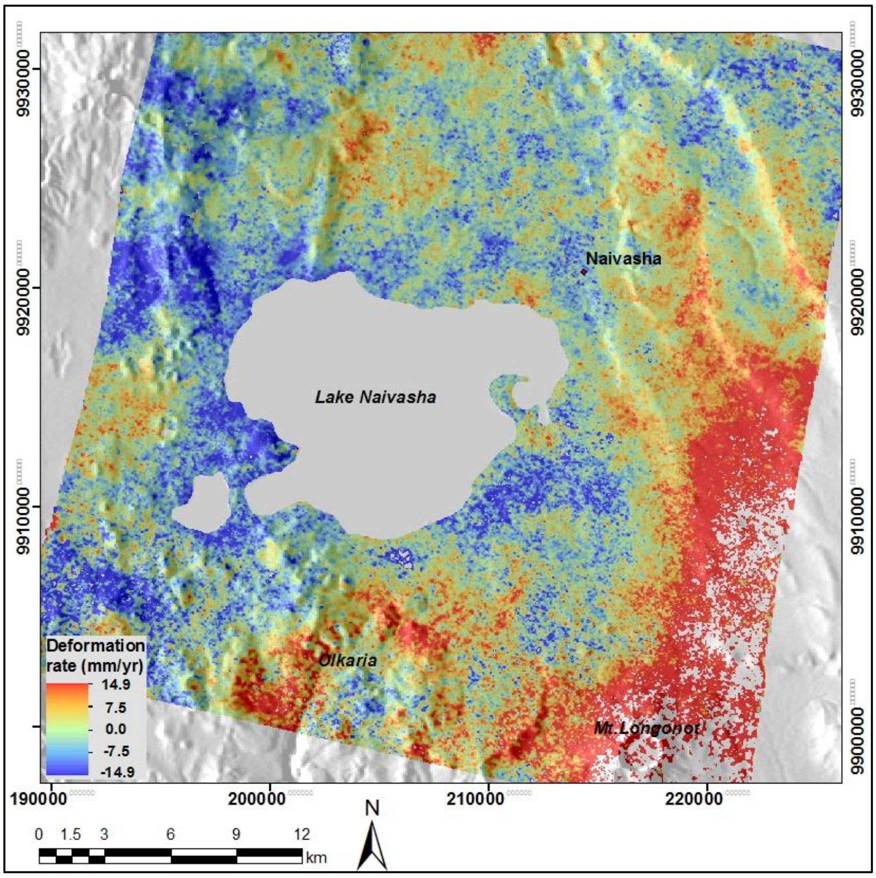

Figure 4.6: The temporal evolution of deformation rate for 5 years observation (2003-2008) using stacking interferogram overlaying with digital elevation model (DEM) SRTM 90m

4.2. Surface active faults interpretation and field work validation

SRTM shaded relief in three direction sun illuminations (45°, 135° and 210°) aims to enhance the image, so that the fault lines along the rift edges can be identified.

Figure 4.7shows the regional surface active faults interpreted from SRTM DEM. Red points refer to the station number carried out in the field where observations were taken (Appendix 1). Regional structures along the rift boundaries (eastern and western of rift floor) were identified as normal faults. Unknown slip direction faults in the rift floor were interpreted as faults. The normal fault with the dextral component (inset in Figure 4.7) was visualized in Figure 4.12. The line features which might be related to the faults were interpreted as the lineaments. From the DEM hill shade image, the topographical features related to the grabens structures were shown on the rift floor in relatively N-S direction bordered by two rift margins.

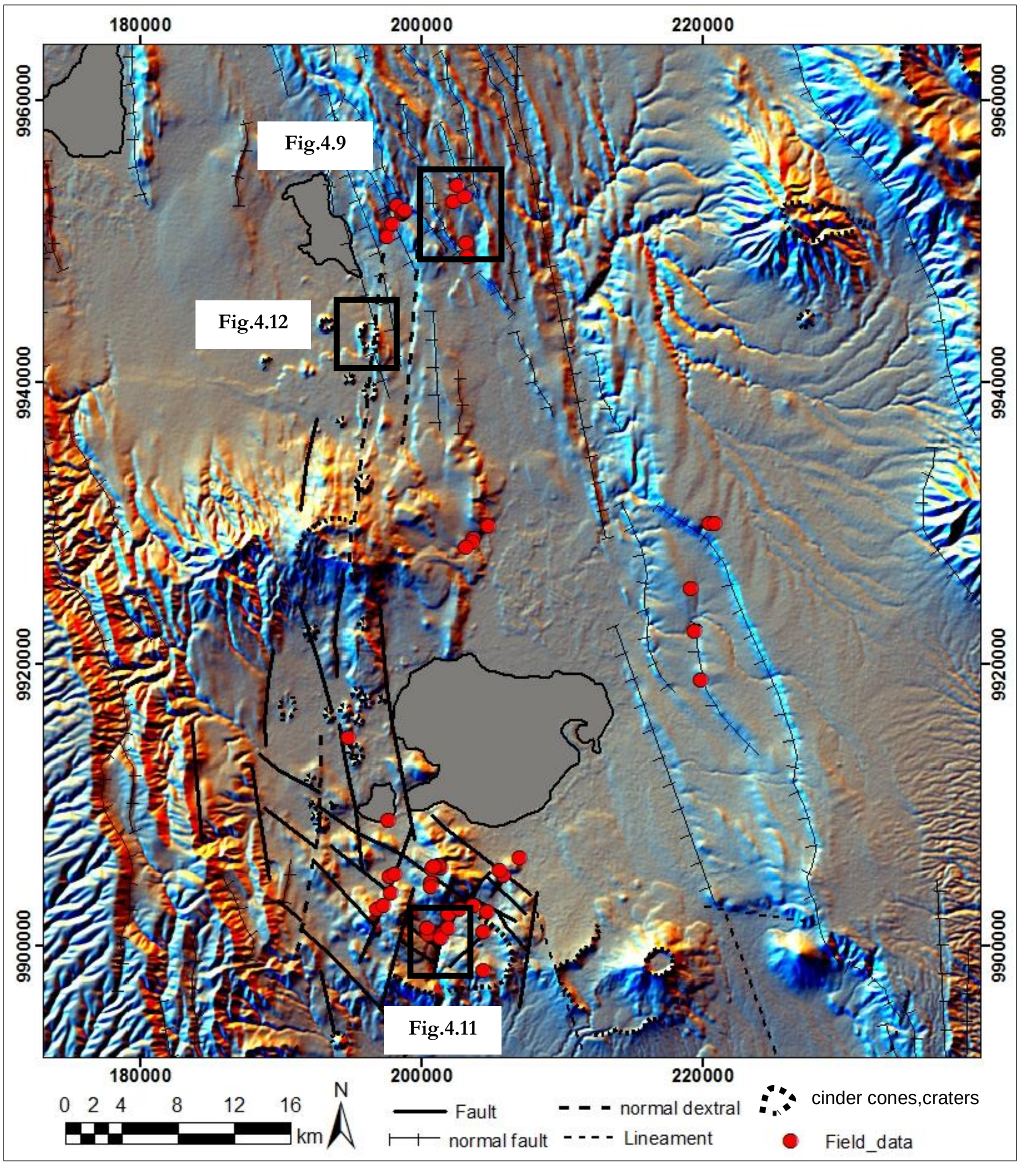

Figure 4.7: Surface structure interpretation from DEM SRTM

Six faults orientation, cinder cones and craters associated with the recent volcanism had been identified through visual interpretation from DEM SRTM as well as in the field. The six faults orientation include: NW-SE, NNW-SSE, N-S, NNE-SSW (major), NE-SW, ENE-WSW (minor). To visualize better, these faults were plotted in a rose diagram (Figure 4.8) showing its length and frequency.

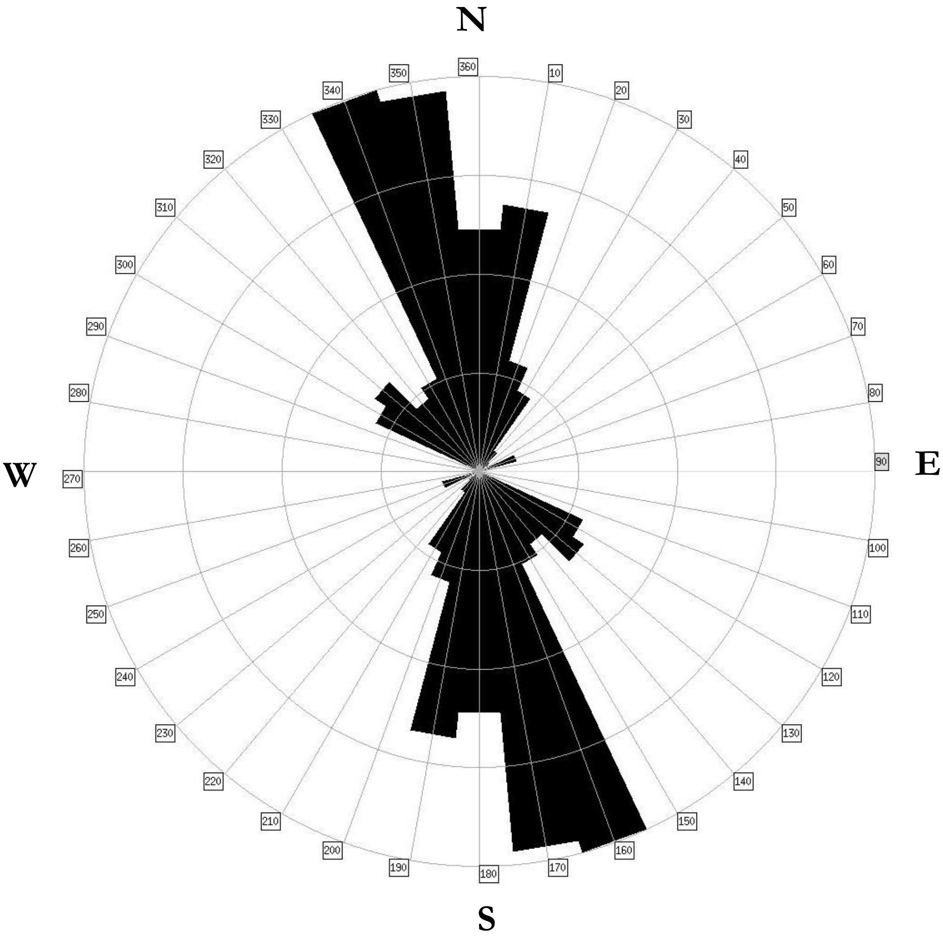

Figure 4.8: The rose diagram represents fault direction and its frequency.
Fault orientations were identified as; NW-SE, NNW-SSE, N-S, NNE-SSW, NE-SW, ENE-WSW.

1. NW-SE &NNW-SSE Fault

NW-SE & NNW-SSE faults orientation were depicted as dissected normal faults featuring graben structures in eastern and western rift margins. Their dipping was almost vertical (around 80°). NNW-SSE faults are more correlated with the recent rift margin than NW-SE faults.

Field observation in the northern part of Lake Naivasha (along the rift margin) reveals the NW-SE trending fault in the Gilgil and Elementaita area (location: NA-11-11) where the escarpment height (apparent displacement) exceeds 10 m (Figure 4.9). It is associated with the hot springs and occurs in the altered rhyolitic rocks mixed with the obsidian fragments (Figure 4.10).

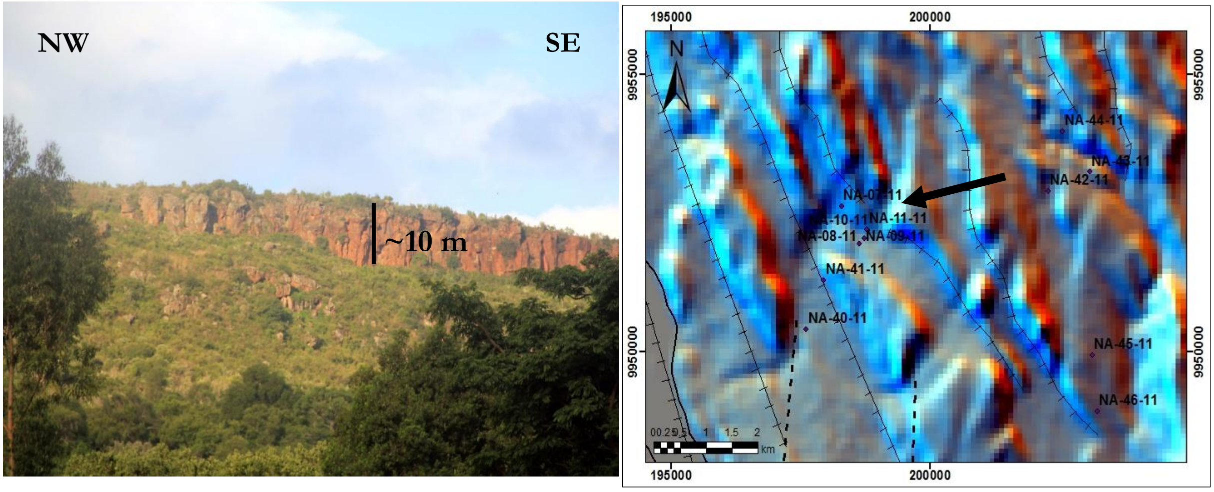

Figure 4.9 : NW-SE fault trend in Gilgil area, eastern rift margin (location NA-11-11)

Figure 4.10 : The altered rhyolitic rocks (left) associated with hot springs close to the location of NA-11-11

Hot springs along the fault trends could be a significant indicator to identify whether the fault is active or not (Delvaux & Barth, 2010). The NW-SE trending fault considered as active might have been re-activated by the closely N-S fault trends. Hot spring was coming out to the surface as a result of the opening of weak zone along such fault trends.

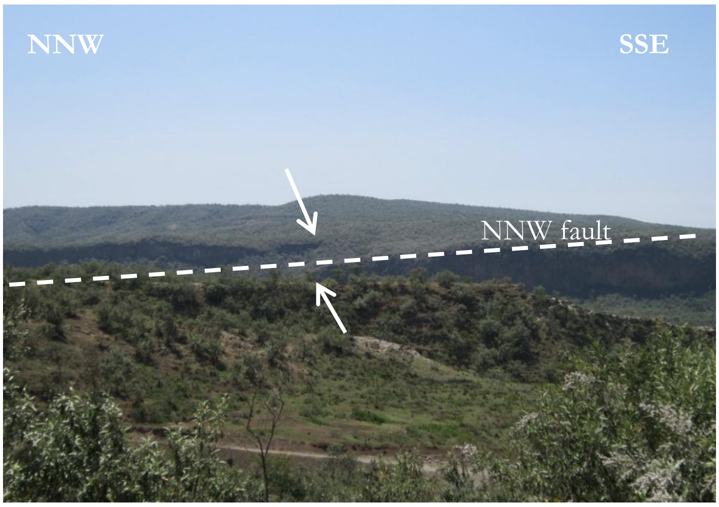

Figure 4.11 :Offset of an escarpment (arrows) by NNW faults observed in Olkaria volcanic complex (Location NA-13-11)

In addition, morphological escarpments associated with fault line were observed in the area of Olkaria Geothermal Field; outcropping as vertical cliff in a rhyolitic lava. They were offset as can be seen in Figure 4.11 (see arrow). This NNW-SSE faulted escarpment complements the observation made from SRTM interpretation.

2. **N-S & NNE-SSW Fault**

The N-S and NNE-SSW trending faults were interpreted mainly along the rift floor. They cross-cut the NW-SE and NNW-SSE faults. Some were recognized as normal fault with dextral component as can be seen in figure 4.12 (inset showing location in Figure 4.7) in the northern area between Lake Naivasha and Lake Elementaita close to Mt. Eburu. This orientation is interpreted as the latest Holocene faults in the area (Strecker, et al., 1990).

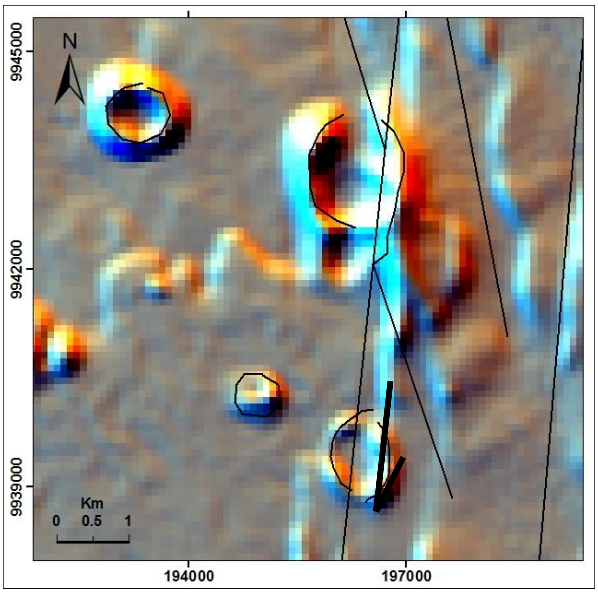

Figure 4.12: Zoomed normal fault with a dextral component

Field observation in Olkaria Geothermal Field confirms the N-S and relatively NNE faults, to be the youngest in the study area. They are active, with the presence of hot springs located within the layered tuff and pyroclastic rock units in the Ol Njorowa Gorge (Figure 4.13).

Figure 4.13 : Vertical layering of tuff and pyroclastic units (left) and the presence of hot spring (right) in Ol Njorowa Gorge, associated with N-S and NNE faults (location:NA-17-11 and NA-16a-11)

Fumaroles were also observed in the Northwest Olkaria Geothermal Complex which supports that the NNE-SSW trending faults are active (Figure 4.14).

Figure 4.14 : Fumaroles outcrop on the altered volcanic rocks aligning NNE fault trends in the Northwest of Olkaria (location NA-38-11a)

3. NE-SW, ENE-WSW Fault

NE-SW and ENE-WSW faults were interpreted mainly located in the Olkaria Geothermal Field. The ENE-WSW trending fault was confirmed with the previous investigation (see Section 2.3.1). During fieldwork, these two fault trends could not be observed.

In Olkaria Geothermal Field (OGF), the four faults trending NW-SE, NNW-SSE, N-S and NNE-SSW were easy to map during the field work, while the NE-SW and ENE-WSW fault trending could not be traced in the field. These structural features can act as a good pathway for fluid flow.

4. Cinder cones and craters

Craters were interpreted based on surface morphology of recent volcanic landform as shown by Mt.Longonot, Mt.Suswa, and Mt. Menengai in northern part of Nakuru. The old volcanic crater was interpreted in the Olkaria Dome. Cinder cones were identified in the Crater Lake situated in eastern part of Lake Naivasha and the eroded dissected old circular patterns covered by recent volcanic product in the northern part of Eburru (Figure 4.12).

4.3. Extracting agriculture features from ASTER image

Figure 4.15 shows the agriculture features which are depicted from the ASTER False Colour Composite (FCC) RGB combination band 321. In this image, the rectangle and circular patterns around the Lake correspond to horticulture agriculture activities. The agricultural areas extend further into the alluvial plain associated with the lake deposit (lacustrine sediment). Also in this image, vegetation cover appears in red. Vegetation cover corresponds to the forest areas are situated in the Northwestern part of the lake occupying the hilly area. While in the low land, vegetation cover associates with the river flow and swampy areas around the Lake. This information, mainly in agriculture features will be used in the data integration part in chapter 5.

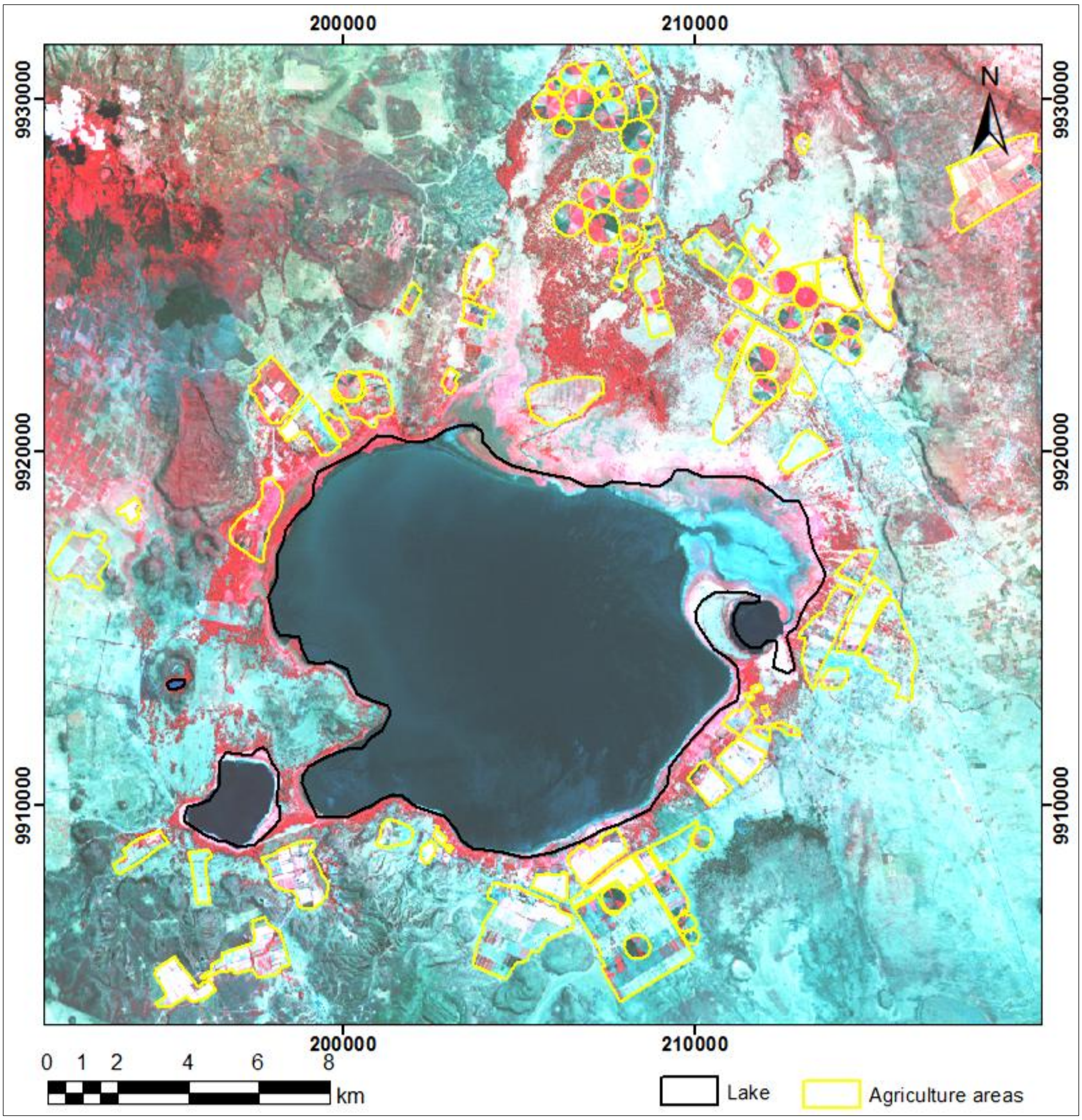

Figure 4.15 : Agricultures areas around the Lake Naivasha, extracted from the ASTER FCC RGB 321

5. DATA INTEGRATION AND ANALYSIS

This chapter discuss the integration of DinSAR surface displacement map combined with extracted information from remotely sensed data analysis and other secondary dataset to analyse and determinate the cause of earth surface deformation in the three possible conditions: 1).Geothermal extraction in the Olkaria Geothermal Field, 2).Groundwater abstraction in agriculture areas surrounding Lake Naivasha and 3). Active faults segments and volcanoes in Kenya Rift Valley.

5.1. Surface deformation observation in Olkaria Geothermal Field

The conventional two-pass DinSAR surface deformation performed in the Olkaria Geothermal Field (OGF) is inadequate. Of the six pairs of DinSAR generated (date from 20031027 to 20080218), only two pairs; namely 20031027 - 20031201 and 20060703 – 20060807, could be considered to offer reliable interferograms in the LOS direction, while the rest were dominated by noise due to temporal decorrelation. The two differential interferogram pairs produced, however, could not adequately be interpreted because the acquisition time interval of 35 days is too small to consider monitoring surface deformation. Besides, no major particular event (earthquake, landslide, etc) is recorded from this area during this period to justify any kind of deformation.

Due to this condition therefore, the surface deformation rate analysed from the stacking interferograms using SBAS technique (Section 4.1.2) is utilized to examine the evolution of deformation in Olkaria Geothermal Field during five years observation (2003-2008).

Figure 5.1 shows the map of ground surface deformation integrated with active production wells, current injection wells, and surface structures denoting active faults in the area. Figure 5.1 does not cover the whole OGF areas. The input SAR images for generating temporal surface deformation were taken from different scenes; and as such, it only captures the Olkaria I, the Olkaria II and the Olkaria Dome respectively.

The ground surface deformation is assumed to be in a vertical motion by neglecting the satellite incident angle (around 23° for Envisat ASAR). As shown in figure 5.1, variation on ground surface deformation occurred in OGF. More uplifting observes in the Olkaria East Field (Olkaria I) than in the Olkaria North East Field (Olkaria II) ranging up to 14 mm/year with approximately 9.4 mm/year in average. While in the Olkaria II, the detected ground surface deformation is ranging from -8 to -13 mm/year of subsidence. Similarly, about -7 mm/year of ground surface deformation is identified in the northern part of Olkaria Dome Field. In some places, the subsidence is estimated to -10 and -12.9 mm/year.

In order to analyse the cause of uplifting in Olkaria I, the geothermal production was integrated to the ground surface deformation map. The production information and the deformation rate were extracted for comparison purposes. Figure 5.2 illustrates the relation between surface deformation rate in the Olkaria I and the geothermal production. Refers to the second hypothesis (Section 1.6) which stated that the more pumping rate in geothermal fluid, the more subsidence are likely to occur. Conversely, as shown in Figure 5.2 the geothermal production is comparable with the presence of uplifting.

As reported by Mariaria (2011), the hot and cold injection wells were installed in the Olkaria I (OW-03 and OW-06) and the Olkaria II (OW-R2, OW-R3,OW-703 and OW-708). Those were installed to prevent the subsidence and to keep the reservoir from cooling. Thus, according to this information, the uplifting occurred in the Olkaria I is likely due to the activities of injection wells.

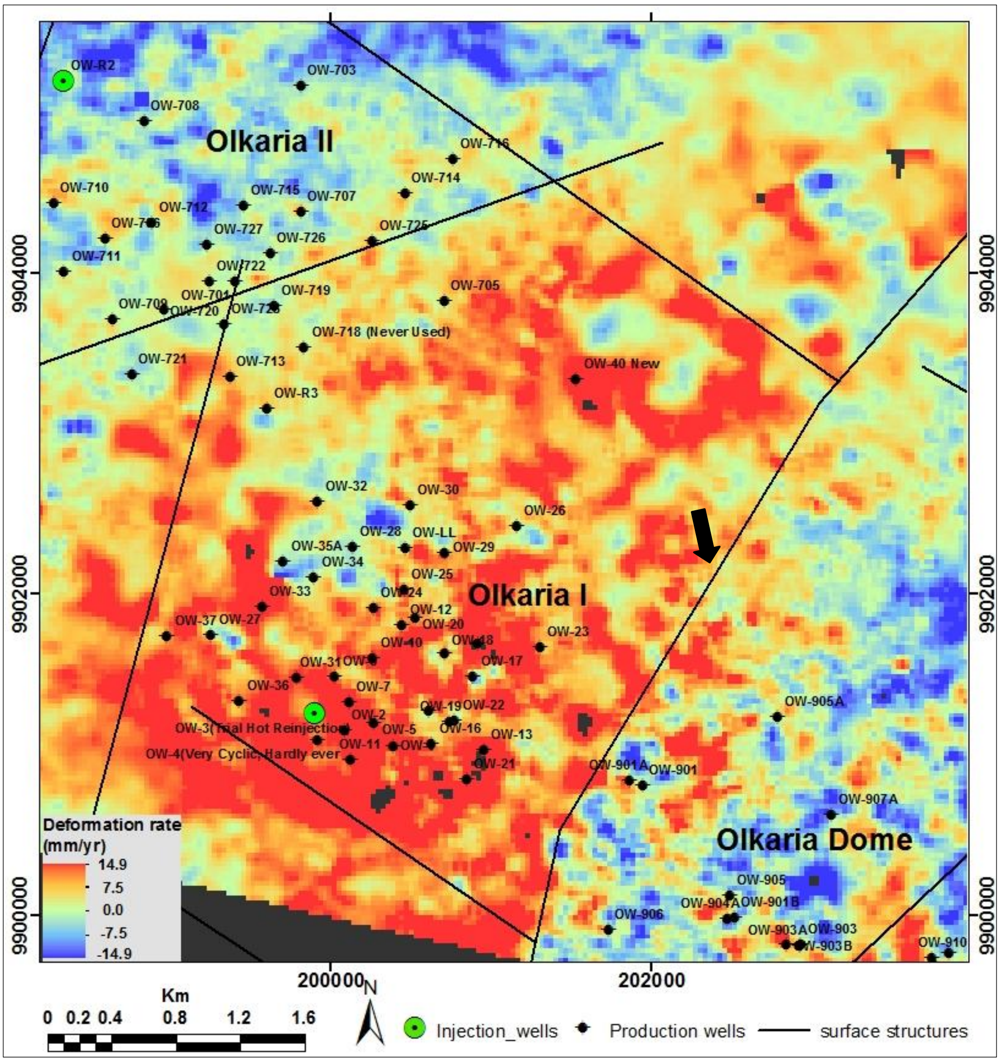

Figure 5.1: Temporal surface deformation rate of Olkaria Geothermal Field from 2003 to 2008.

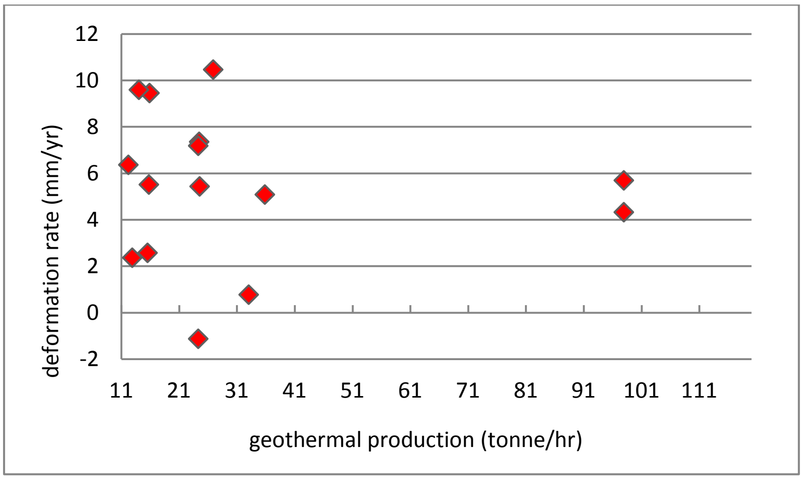

Figure 5.2: Surface deformation rate and geothermal production in the Olkaria I from 2003 to 2008; upper zero (uplifting), below zero (subsidence)

To analyze the contribution of the surface structures to ground deformation, the active faults within the Olkaria Geothermal Field were taken into consideration. In this case, the active fault trending NNE aligning Oljorowa Gorge (see by arrow in figure 5.1, possibly control the ground deformation in the field. The relative uplifting and subsidence observed from ground deformation map coincides this fault. Field observation confirmed this fault to be active and marked by the presence of hot springs along its trace which is outcropping in layered tuff formation (location NA-16a-11; see Figure 4.13; Appendix 1).

From the temporal surface deformation rate map (Figure 5.1), the pattern (trending NE) of the uplifting area in the Olkaria-I is parallel to the bounding NE&NNE faults. This uplifted area looks like a horst structure and possibly vertical dipping. This structure is favourable for heat flow pathway. Considering the Olkaria geothermal system is strongly controlled by the structures (Muchemi, 1999; Omenda, 1998), the integrated deformation map with the structures shows the NE&NNE trending deformation pattern possibly can be used to identify possible geothermal source within unexplored areas.

Discussion

The ground surface deformation rate has been processed from the multitemporal stacked differential interferogram through SBAS method. It was recorded at around 14 mm/year of uplifting and -13 mm/year of subsidence in the Olkaria Geothermal Field. The deformation rate in the study area was found relatively lower than the other geothermal fields outside Africa (due to lacking of surface deformation studies in Africa geothermal fields) e.g. it is about 5 cm/year in Reijecnik Field, Iceland (Keiding et al., 2010) and up to 5 m in New Zealand (Hole, et al., 2007).

The observed ground surface deformation in Olkaria Geothermal Field is still reliable. However, this result needs to be validated with the ground truth deformation measurement from high precision GPS (Geodetic Levelling GPS) which is ongoing observation in 2011 until the next four years (Koros, 2011, personal communication).

5.2. Surface deformation observation related to groundwater extraction

Ground surface deformation from stacked interferogram indicates subsidence around the Lake Naivasha area. The rate of deformation recorded at maximum of ± 15 mm/year and about -7 to -10 mm/year in average is considered as slow rate deformation. To validate this result, the integration of other data such as temporal groundwater level measurement and land use information over the areas investigated were used.

Figure 5.3 shows the groundwater fluctuation level for the period 1999-2001-2004 obtained from thirty locations run by agricultures companies surrounding Lake Naivasha. Although the groundwater level measurement does not coincide with the data used for surface deformation (study in the area e.g 2006 - 2008), the declining trend in some wells observed was assumed to be similar with this measurement.

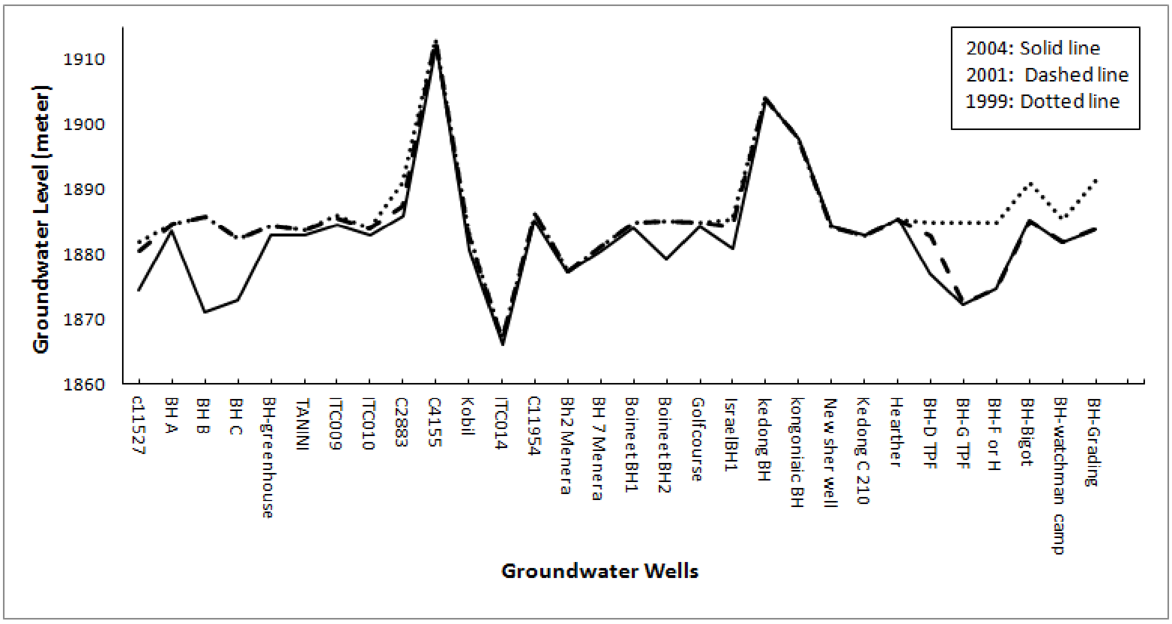

Figure 5.3: Temporal groundwater level measurement in 1999-2001-2004 surrounding Lake Naivasha

Figure 5.4 shows the surface deformation map overlays with location of the wells for groundwater level measurement and agricultures area which are interpreted from the ASTER False Colour Composite RGB combination of band 321 (see Figure 4.15).

Most of the relative subsidence is located in the surrounding of Lake Naivasha. These areas are spatially correlated with the agriculture areas. The surface deformation (subsidence) within these farming lands, therefore, can be interpreted as groundwater abstraction induced.

Even though not all the location of groundwater extraction show subsidence, the decreasing groundwater level known from two wells located in the western part of Lake Naivasha do compliment the surface deformation (e.g; Boinnet BH1 & Boinnet BH2, in Figure 5.5, and inset in figure 5.4) (Kibona, 2000; Nabide, 2002; Yihdego, 2005) recorded at about -8 mm to -10 mm/year of subsidence by the current method.

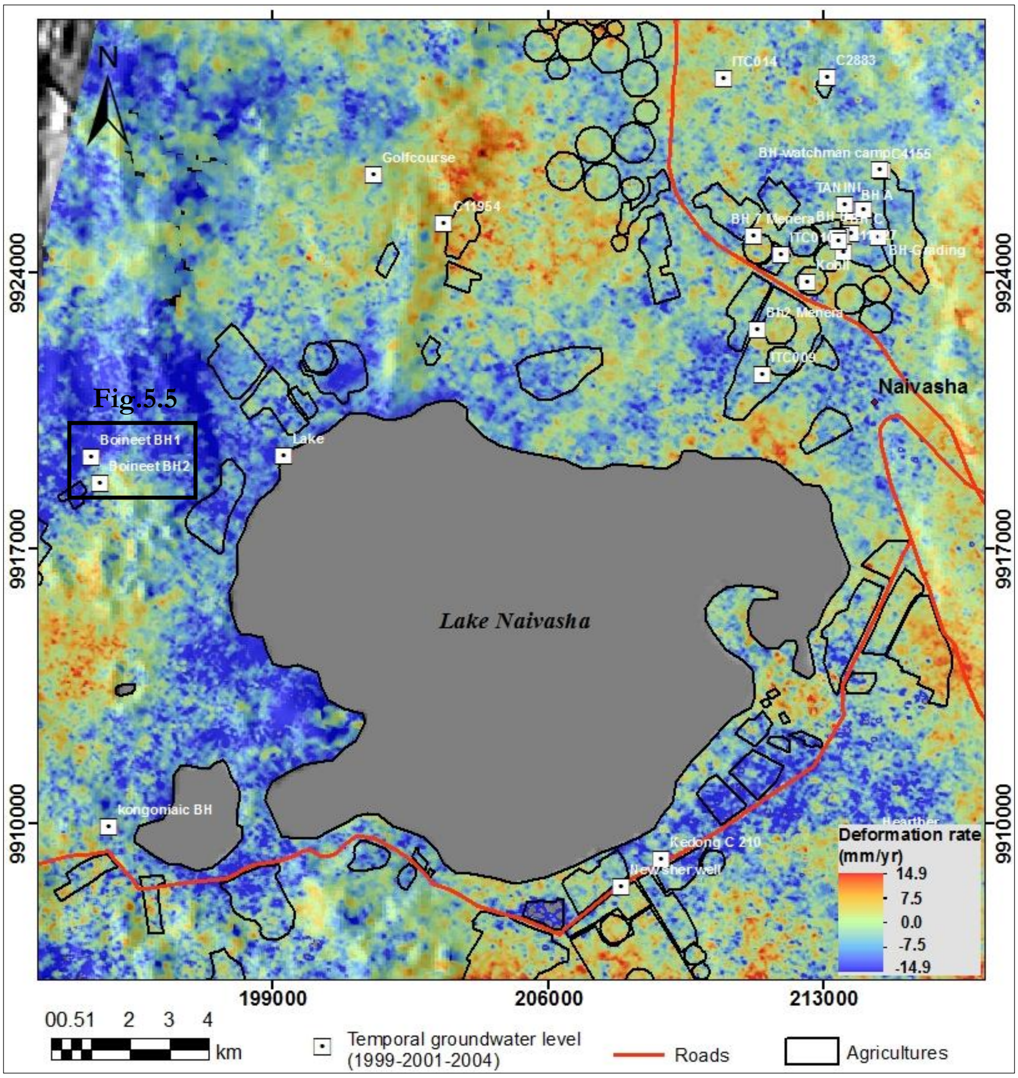

Figure 5.4: Slow rate deformation evolution from 2003 to 2008 around Lake Naivasha

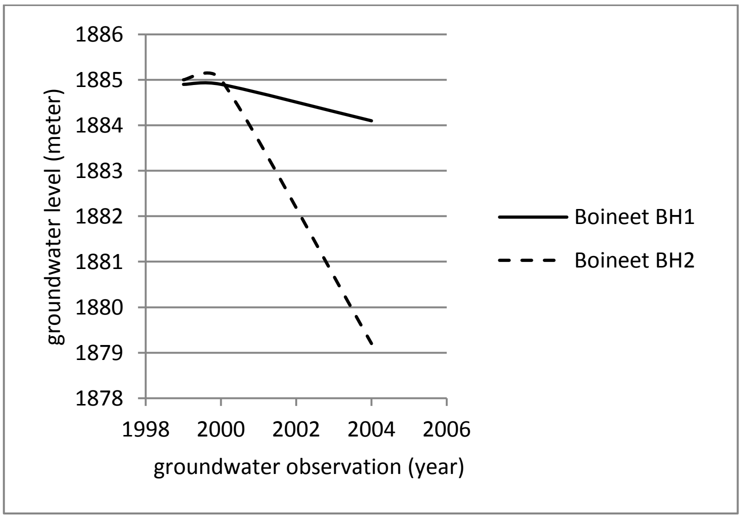

Figure 5.5: Groundwater decreasing level at Western part of Lake Naivasha

Discussion

Observation on surface deformation in Lake Naivasha and the surrounding area has identified some subsidence patterns which are coincided with the agriculture activities. The groundwater level measurement over the agricultural companies surrounding Lake Naivasha showed over 3 meters decreasing trends from 1999 until 2004 (see Section 2.4). These decreasing trends confirm the idea that the current subsidence that occurred in the Lake Naivasha is relatively caused by groundwater extraction.

Data integration also allows the subsidence validation by comparing the area of subsidence, from the surface deformation map, with the decreasing trends on groundwater level measurement. Only two wells (Boinnet BH1 & Boinnet BH2) conform to the subsidence pattern in the surface deformation map whereas the other wells don't exhibit any correlation due to the no/less decreasing trend in groundwater levels.

Regarding the image acquisition during InSAR processing, seasonal changing might effect on soil moistures. Six images used for InSAR surface deformation was taken during rainy season (see Section 3.1.1). Thus, the small changing on mm scale is probably due to compaction and swelling of clay content. This is supported by the fact that the areas surrounding the Lake Naivasha are covered by lacustrine sediments which is dominated by sandy-clayed soils (see Section 2.2).

5.3. Surface deformation observation related to tectonic activities

The study area is situated in the KRV zone which is tectonically active. The possible regional geodynamic contribution to the observed deformation over the study area and its surrounding needs to be considered. The surface displacement map taken from the time series of conventional DinSAR analysis doesn't result in sufficient interferogram fringes (see Section 4.1.1.3) due to temporal decorrelation during five years observation (2003-2008). However, one pair of surface displacement map, spanning 20070305 – 20080218 shows sufficient interferogram fringes that can be interpreted.

Figure 5.6 illustrates the regional surface displacement which is integrated with interpreted surface active faults. Inset map shows the coverage of the study area compare with the regional view of Kenya rift valley.

The number of fringes in full colour cycle (blue-green-yellow-red) is used to interpret the surface displacement along the satellite line of sight (LOS). One cycle of colour fringe is occurred in the image and it is equal to the 28 mm (2.8 cm) of subsidence according to the line of sight direction (LOS in red arrow, figure 5.6). The observed colour fringe is very clear compare to the rift borders which is dominated by noise. It spreads along the rift floor trending NNW-SSE parallel to the active faults segments (white lines). According to this figure, the deformation in this rift floor environment is considered still to be active during one year observation (2007-2008).

This result, however, is much lower compare to InSAR study of ground deformation on 2007 in immature continental rift environment located in Northern Tanzania which was recorded at 40 cm of subsidence related to the active fault on NE striking fault and dyke extension (Biggs et al., 2009). Yet, the value might be varies considering the dynamic of continental rift environment.

To analyze further whether the recent tectonic activities contributes to the surface deformation in KRV, a surface displacement map is created from the unwrapped interferogram (figure 5.6) in the area of high coherence value to minimize the noise. Flat areas, relatively less vegetation and homogenous topography then are chosen to avoid any error contribution.

Figure 5.7 shows the result of displacement map (black rectangle map in figure 5.6) which is combined with the recent tectonic activities represented by N-S trending faults. The displacement profile illustrated that during one year observation of relatively vertical displacement, at approximately 0.006 m which is equal to around 6 mm, was occurred within this line. This fault is considered as normal fault with some dextral movement (as interpreted in Section 4.2)

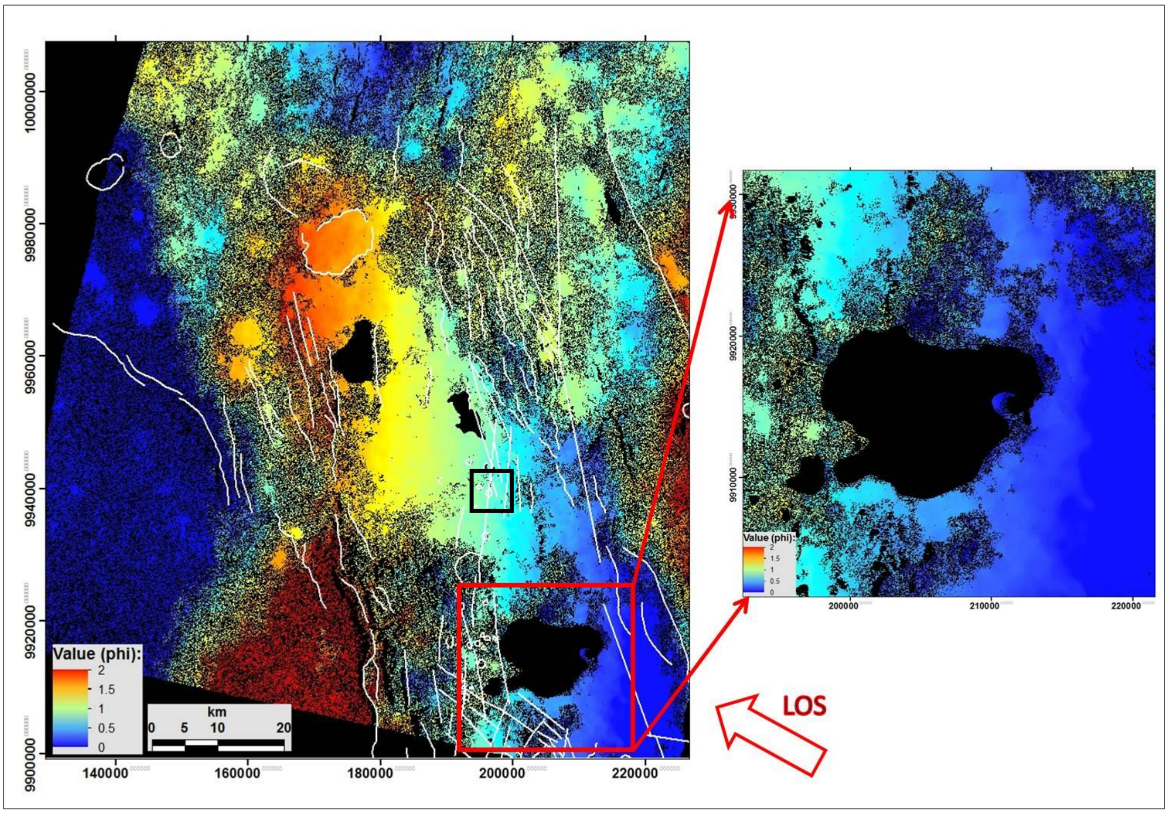

Figure 5.6: The surface displacement according to Line of sight (LOS) satellite direction using unwrapped minimum cost flow algorithm. The slow movement detected in one full colour fringes equal to 28 mm showing subsidence along the rift floor. The DinSAR acquisition is 1 year (20070305-20080218), the white line is interpreted active fault segment along the rift system.

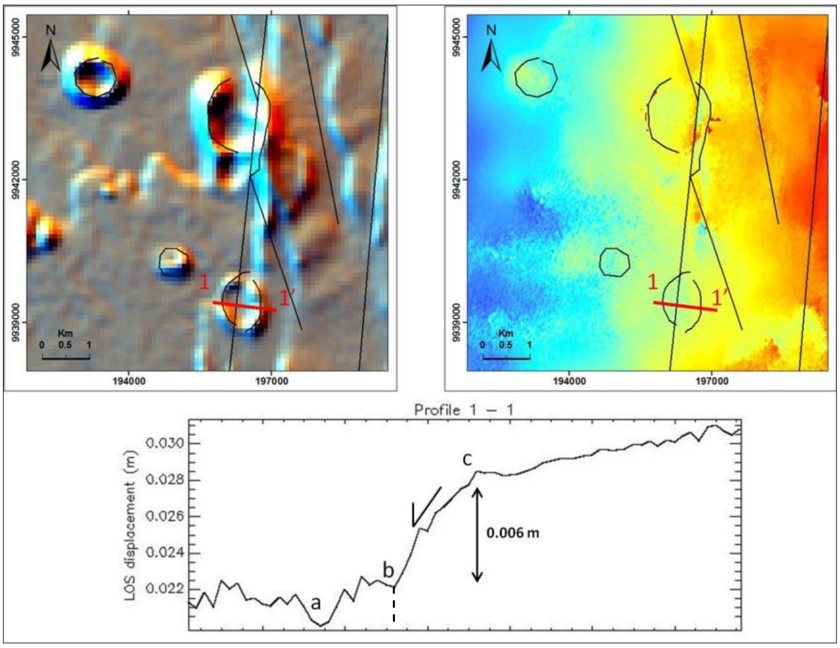

Figure 5.7: Active deformation profile along the relative N-S fault trends detected from surface displacement along Line-of-Sight (LOS) in one year period (2007-2008).

In addition, the surface deformation rate using stacked interferogram method (SBAS) was analyzed to identify the tectonic activities associated with active fault segments and volcanoes.

Mt. Longonot, located in the southeast of Lake Naivasha, shows uplifting in the range of 5 to 15 mm/year and this is considered as the highest among the other areas (Biggs J., et al., 2009). The extension part of Mt. Longonot to the eastern rift border, which is aligning the NNW-SSE active fault segments, exhibits the same uplifting while small craters in the western part of Lake Naivasha do not show deformation during five years of observation

The relative deflation (subsidence) features in the western part of the study area are coincides with the N-S active fault segments that are situated in the middle part of the rift floor (it is situated in the Northwestern part of Lake Naivasha, in Figure 5.8).

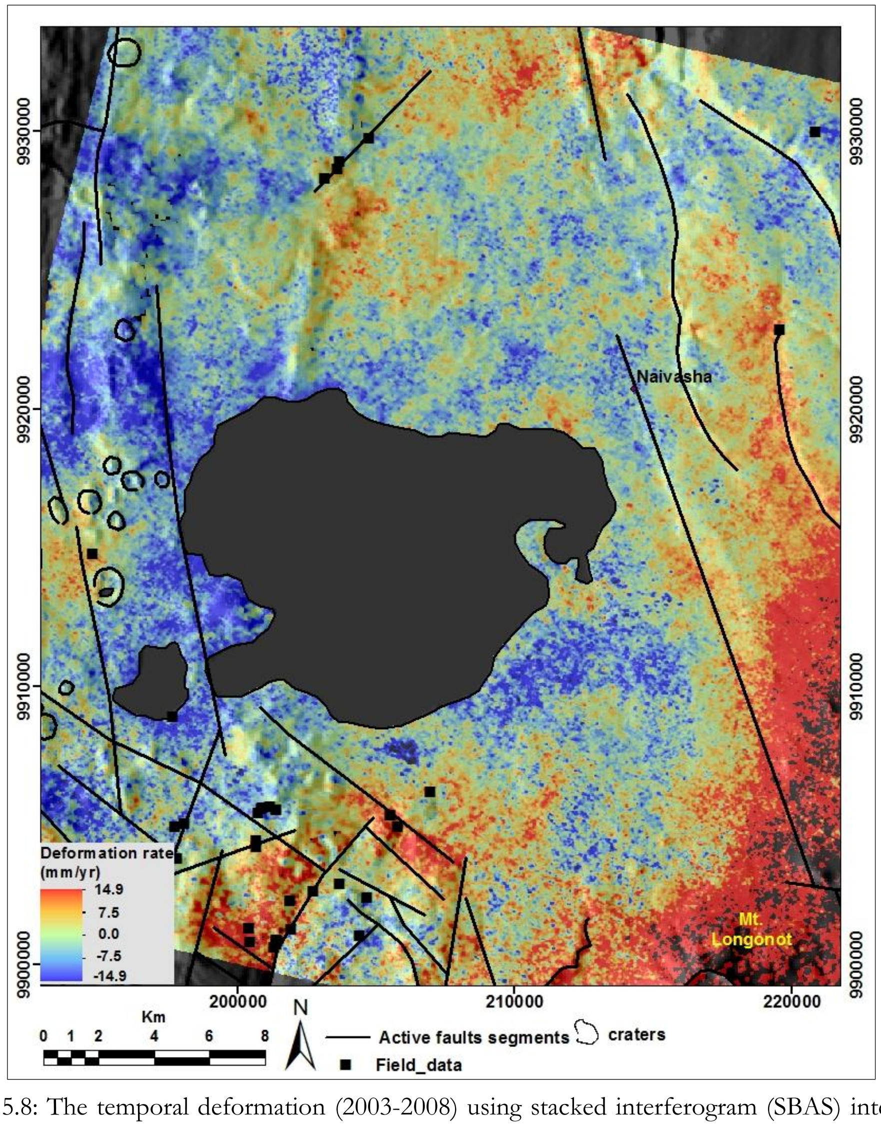

Figure 5.8: The temporal deformation (2003-2008) using stacked interferogram (SBAS) integrated with active faults segments and active volcanoes. Field data were done to validate these active faults

Comparison result is made between surface deformation from conventional DinSAR in one year observation (2007 – 2008) and the temporal surface deformation rate from interferogram stacking. Surface deformation from DinSAR is recorded at 28 mm subsidence along the rift floor in NW-SE direction. From that value, the local surface deformation over the active fault segments within the study area (inset picture in figure 5.6) is inferred at approximately 0.25π which is equal to 7 mm for one year observation. This result is slightly different compare to the deformation result from interferogram stacking which is recorded at around 7 to 12 mm/year. Yet, these two results need to be validated with ground truth of GPS measurement.

Discussion

The ground surface inflation observation of the active volcano Mt. Longonot using stacked interferogram was approximately 7.5 cm of maximum uplifting within five years period (2003-2008). This number is relatively smaller than what was measured by Brigg et.al, (2009) on the same volcano of about 9 cm in the period of 2004-2006 (see Section 2.5.4). This number might vary considering the surface deformation is changing in time and space.

Uplifting activities might be related to the shallow magmatic intrusion associated with the opening crust in the continental rift floor environment (Chorowicz, 2005).

The ground surface deformation observed from both two-pass differential interferogram and stacking interferogram (SBAS) methods were found conformable with the surface active faults (Figures 5.7 & 5.8). In addition to the hotsprings and fumaroles evidence as described in the previous section; some measurements that were taken from the field such as offset and apparent displacements along escarpments (Figures 4.9, 4.11 & Appendix 1) also indicate that these faults are active and as a consequence they contribute in the surface deformation.

6. CONCLUSION AND RECOMMENDATION

6.1. Conclusions

In reference to the research questions raised in chapter 1, the following conclusions could be made:

- Research question 1: **"Is the technique robust enough to determine where surface deformation could have occurred?**

  Differential Interferometry (DInSAR) using SBAS (small baseline subset) technique is able to map multi-temporal slow rate surface deformation in the study area. Conventional two-pass DinSAR, however, could not be applied properly. This probably due to decorrelation effects in longer time acquisition and also other technical and natural effects such as atmospheric condition and seasonal condition that might effects SAR quality images in the study area.

- Research question 2: **"Can the causation of surface deformation in the Olkaria Geothermal field be determined?"**

  Both injection wells activities and structural behaviour contributing to the surface deformation occurred in Olkaria Geothermal Field.

- Research question 3:**"Can the causation of surface deformation around Lake Naivasha be determined?"**
  The temporal surface deformation occurred around Lake Naivasha is possibly due to groundwater abstraction as it is associated with the floral farming activities surrounding the lake. But, more uncertainties still occur due to unavailability of groundwater level measurement in this area that might give indication of subsidence.
- Research question 4: **"Can the causation of surface deformation related tectonic activities be determined?**
  Based on the stacking interferogram using SBAS for five years observation (2003-2008), the surface deformation could be determined as a result of the Mt.Longonot volcano and the active faults. Whereas based on the two-pass differential interferogram method for one year observation (2007 to 2008), the surface deformation could be related to only the active faults.

6.2. Recommendation

- Due to two years missing in the InSAR dataset (2004&2005) and then the results might be not representative, long period and continuous InSAR dataset (more-less taken in the same seasonal period of the year, preferably dry season, to avoid the temporal effects) should be acquired to monitor surface deformation in the study area.

- Differential interferogram (DinSAR) processing and analysis in this study somehow contains uncertainties due to noise and error caused by geometrical and interpolation error during phase unwrapping. Prior knowledge of the expected subsidence rate within the area is necessary to take into consideration.

- Despite the limitation of the obtained result, the stacked interferogram, which I applied for this study, is still feasible. To detect the slow rate of deformation within the agriculture area, it is recommendable to put artificial corner reflectors in some reference points of the area of interest (Hanssen, 2001).

- Since the surface deformation is based on satellite line-of-sight (LOS) direction in descending mode, It is recommended to use both direction (ascending and descending mode) in the future for a good understanding of the surface deformation the study area .
- The SAR image in longer wavelength (L-band); e.g ALOS Palsar, for InSAR generation, is desirable to penetrate the vegetation cover and minimize the atmospheric effects during multitemporal surface deformation monitoring and should be considered in future investigations.
- Continuity measurement of conventional surface deformation method, e.g, geodetic levelling GPS, is highly recommended to validate the result from multitemporal DinSAR surface deformation in the study area.
- The continuity of groundwater level monitoring is significant to validate the DinSAR surface deformation around the floral farms which shows deflation in these areas.

LIST OF REFERENCES

Becht, R., & Nyaoro, J. R. (2005). influence of groundwater on lake - water management : the Naivasha case. *In: Proceedings of the 11th world lakes conference, 31 October - 4 November 2005, Nairobi, Kenya. Nairobi : Ministry of Water and Irrigation ; International Lake Environment Committee (ILEC), 2006. Vol. II. pp. 384-388.*

Berardino, P., Fornaro, G., Lanari, R., & Sansosti, E. (2002). A new algorithm for surface deformation monitoring based on small baseline differential SAR interferograms. *Geoscience and Remote Sensing, IEEE Transactions on, 40*(11), 2375-2383.

Bertani, R. (2005). World geothermal power generation in the period 2001-2005. *Geothermics, 34*(6), 651-690.

Biggs, J., Amelung, F., Gourmelen, N., Dixon, T. H., & Kim, S. W. (2009). InSAR observations of 2007 Tanzania rifting episode reveal mixed fault and dyke extension in an immature continental rift. *Geophysical Journal International, 179*(1), 549-558.

Biggs J., Anthony E.Y., & Ebinger C.J. (2009). Multiple inflation and deflation events at Kenyan volcanoes, East African Rift. *Geological Society of America.*

Chang, H. C., Ge, L. L., Rizos, C., & Ieee. (2005). *InSAR and mathematical modelling for measuring surface deformation due to geothermal water extraction in New Zealand.* New York: Ieee.

Chlieh, M., de Chabalier, J. B., Ruegg, J. C., Armijo, R., Dmowska, R., Campos, J., et al. (2004). Crustal deformation and fault slip during the seismic cycle in the North Chile subduction zone, from GPS and InSAR observations. *Geophysical Journal International, 158*(2), 695-711.

Chorowicz, J. (2005). The East African rift system. *Journal of African Earth Sciences, 43*(1-3), 379-410.

Costantini, M. (1998). A novel phase unwrapping method based on network programming. *Ieee Transactions on Geoscience and Remote Sensing, 36*(3), 813-821.

Costantini, M., & Rosen, P. A. (1999). *A generalized phase unwrapping approach in sparse data.* Paper presented at the IGARSS, Hamburg, Germany,June 1999.

Delvaux, D., & Barth, A. (2010). African stress pattern from formal inversion of focal mechanism data. *Tectonophysics, 482*(1-4), 105-128.

Dimitrios, G. (1989). *Magnetotelluric studies in geothermal areas in Greece and Kenya.* Ph.D Thesis, University of Edinburg.

Drury, P. (2001). *Image Interpretation in Geology* (3 ed.). Canada: Blackwell Science.

European Space Agency. (2011). RADAR and SAR Glossary. Accessed on : http://envisat.esa.int/handbooks/asar/CNTR5-2.htm

Ferretti, A., Prati, C., & Rocca, F. (2001). Permanent scatterers in SAR interferometry. *Ieee Transactions on Geoscience and Remote Sensing, 39*(1), 8-20.

Fialko, Y., & Simons, M. (2000). Deformation and seismicity in the Coso geothermal area, Inyo County, California: Observations and modeling using satellite radar interferometry. *Journal of Geophysical Research B: Solid Earth, 105*, 21,781-721,793.

Fridleifsson, I. B. (2001). Geothermal energy for the benefit of the people. *Renewable and Sustainable Energy Reviews, 5*(3), 299-312.

Fridleifsson, I. B., & Freeston, D. H. (1994). GEOTHERMAL-ENERGY RESEARCH-AND-DEVELOPMENT. *Geothermics, 23*(2), 175-214.

Furgerson, R. B. (1972). *Electrical Resistivity Survey of the Olkaria Project, Kenya.*: EAP&L Geothermal Exploration Project.

Glowacka, E., Sarychikhina, O., Suárez, F., Nava, F., & Mellors, R. (2010). Anthropogenic subsidence in the Mexicali Valley, Baja California, Mexico, and slip on the Saltillo fault. *Environmental Earth Sciences, 59*(7), 1515-1524.

Goldstein, R. M., & Werner, C. L. (1998). Radar interferogram filtering for geophysical applications. *Geophys. Res. Lett., 25*(21), 4035-4038.

Goudarzi, M. A. (2010). *Detection and measurement of land deformations caused by seismic events using InSAR, sub - pixel correlation and inversion techniques.* University of Twente Faculty of Geo-Information and Earth Observation ITC, Enschede.

Han, Y. F., Song, X. G., Shan, X. J., Qu, C. Y., Wang, C. S., Guo, L. M. (2010). Deformation monitoring of Changbaishan Tianchi volcano using D-InSAR technique and error analysis. *Chinese Journal of Geophysics-Chinese Edition, 53*(7), 1571-1579.

Hanssen, R. F. (2001). *Radar Interferometry: Data Interpretation and Error Analysis*: Kluwer Academic Publisher.

Hoen, E. W., & Zebker, H. A. (2000). *Topography-driven variations in backscatter strength and depth observed over the Greenland ice sheet with InSAR*. New York: IEEE
Hole, J. K., Bromley, C. J., Stevens, N. F., & Wadge, G. (2007). Subsidence in the geothermal fields of the Taupo Volcanic Zone, New Zealand from 1996 to 2005 measured by InSAR. *Journal of Volcanology and Geothermal Research, 166*(3-4), 125-146.
Hollnack, D., & Stangl, R. (1998). The seismicity related to the southern part of the Kenya Rift. *Journal of African Earth Sciences, 26*(3), 477-495.
Keiding, M., Arnadottir, T., Jonsson, S., Decriem, J., & Hooper, A. (2010). Plate boundary deformation and man-made subsidence around geothermal fields on the Reykjanes Peninsula, Iceland. *Journal of Volcanology and Geothermal Research, 194*(4), 139-149.
Keller, G. R., Prodehl, C., Mechie, J., Fuchs, K., Khan, M. A., Maguire, P. K. H., et al. (1994). The East African rift system in the light of KRISP 90. *Tectonophysics, 236*(1-4), 465-483.
Ketelaar, V. B. H. G. (2009). *Satellite Radar Interferometry Subsidence Monitoring Techniques* (Vol. 14): Springer Netherlands.
Kibona, S. R. (2000). *Temporal and spatial variation of groundwater level north of Lake Naivasha,Kenya-analysed using modflow*. MSc Thesis, ITC The Netherlands.
Kuria, Z. N. (2011). *Seismotectonics of Active Faults:Magadi fault system, southern Kenya Rift*. PHd Thesis, Faculty of Geo-Information Science and Earth Observation, University of Twente, The Netherlands.
Kuria, Z. N., Woldai, T., van der Meer, F. D., & Barongo, J. O. (2010). Active fault segments as potential earthquake sources: Inferences from integrated geophysical mapping of the Magadi fault system, southern Kenya Rift. *Journal of African Earth Sciences, 57*(4), 345-359.
Maguire, P. K. H., Shah, E. R., Pointing, A. J., Cooke, P. A. V., Khan, M. A., & Swain, C. J. (1988). The seismicity of Kenya. *Journal of African Earth Sciences (and the Middle East), 7*(7-8), 915-923.
Maguire, P. K. H., Swain, C. J., Masotti, R., & Khan, M. A. (1994). A crustal and uppermost mantle cross-sectional model of the Kenya Rift derived from seismic and gravity data. *Tectonophysics, 236*(1-4), 217-249.
Mariaria, J. (2011). *Hot and Cold Reinjection:Olkaria Experience*. Paper presented at the Kenya Geothermal Conference, Nairobi, Kenya.
Mariita, N. O. (2000). *Application of Precision Gravity Measurement to Reservoir Monitoring of Olkaria Geothermal Field, Kenya*. Paper presented at the World Geothermal Congress.
Mburu, M. N. (2007). *Reservoir Engineering Status Report on Steam Production (Assessment of the Reservoir and Steam Status in Olkaria East Field)*: Kenya Electricity Generating Company Ltd.
Mechie, J., Keller, G. R., Prodehl, C., Gaciri, S., Braile, L. W., Mooney, W. D., et al. (1994). Crustal structure beneath the Kenya Rift from axial profile data. *Tectonophysics, 236*(1-4), 179-200.
Muchemi, G. G. (1999). *Conceptualized Model of The Olkaria Geothermal Field*. Naivasha: Kenya Electricity Generating Compay Limited (KenGen).
Mwangi, M. N. (1986). *Interpretation of additional sounding data at Olkaria*: KPC Ltd.
Nabide, I. K. (2002). *Development of 3-D cpnceptual hydrogeological model for Lake Naivasha area:based on the intergaration of geology,hydrochemistry,isotopic analysis and boundary conditions*. MSc Thesis, ITC, The Netherlands.
Ndobi, J. M. (1981). The Structure of the Shallow Crust benarth the Olkaria Geothermal Field, Kenya, deduced from gravity studies. *Jurnal of Volcanological and Geothermal*(9), 237-251.
Oduor, J. A. (2010). *Environmental and Social Consideration in Geothermal Development*. Paper presented at the FIG Congress Environment and Energy : Policy and Practice, Sydney, Australia, 11-16 April 2010.
Olivier, M. (2011). A simple continental rift classification. *Tectonophysics, 513*(1-4), 88-95.
Omenda, P. A. (1998). The geology and structural controls of the Olkaria geothermal system, Kenya. *Geothermics, 27*(1), 55-74.
Onacha, S. A. (1989). *An Electrical Resistivity study of the area between Mt.Suswa and the Olkaria Geothermal Field, Kenya*. MSc Thesis, University of Nairobi.
Ouma, P. A. (2005). *Reservoir Engineering and Geothermal Power Production in Olkaria*. Paper presented at the Workshop for Decision Makers on Geothermal Projects and Management, Naivasha, Kenya, 14-18 November 2005
Riaroh, D., & Okoth, W. (1994). The geothermal fields of the Kenya rift. *Tectonophysics, 236*(1-4), 117-130.
Samsonov S., Tiampo K., Joyce K., Scott B., & Bromley S. (2009). *Modified Stacking and SBAS Algorithms for Mapping of Ground Deformation in Taupo Volcanic Zone, New Zealand with ALOS Palsar*. Paper presented at the ESA Fringe 2009 Workshop.

Simiyu, S. M. (2010, 25-29 April 2010). *Status of Geothermal Exploration in Kenya and Future Plans for Its Development.* Paper presented at the World Geothermal Congress 2010, Bali, Indonesia.

Simiyu, S. M., & Keller, G. R. (2000). Seismic monitoring of the Olkaria Geothermal area, Kenya Rift valley . *Journal of Volcanology and Geothermal Research, 95*(1-4), 197-208.

Simiyu, S. M., & Keller, G. R. (2001). An integrated geophysical analysis of the upper crust of the southern Kenya rift. *Geophysical Journal International, 147*(3), 543-561.

Skobelev, S. F., Hanon, M., Klerkx, J., Govorova, N. N., Lukina, N. V., & Kazmin, V. G. (2004). Active faults in Africa: a review. *Tectonophysics, 380*(3-4), 131-137.

Stramondo, S., Moro, M., Tolomei, C., Cinti, F. R., & Doumaz, F. (2005). InSAR surface displacement field and fault modelling for the 2003 Bam earthquake (southeastern Iran). *Journal of Geodynamics, 40*(2-3), 347-353.

Strecker, M. R., Blisniuk, P. M., & Eisbacher, G. H. (1990). Rotation of extension direction in the central Kenya Rift. *Geology, 18*(4), 299-302.

Tongue, J. A., Maguire, P. K. H., & Young, P. A. V. (1992). Seismicity distribution from temporary earthquake recording networks in Kenya. *Tectonophysics, 204*(1-2), 71-79.

Walling, M. Y., & Mohanty, W. K. (2009). An overview on the seismic zonation and microzonation studies in India. *Earth-Science Reviews, 96*(1-2), 67-91.

Wei, M., Sandwell, D., & Smith-Konter, B. (2010). Optimal combination of InSAR and GPS for measuring interseismic crustal deformation. *Advances in Space Research, 46*(2), 236-249.

Woldai, T., Oppliger, G., & Taranik, J. (2009). Monitoring dewatering induced subsidence and fault reactivation using interferometric synthetic aperture radar. *International Journal of Remote Sensing, 30*(6), 1503-1519.

Yihdego, Y. (2005). *A three dimensional groundwater model of the aquifer around Lake Naivasha area,Kenya.* MSc Thesis, ITC, The Netherlands.

Yonezawa, C., & Takeuchi, S. (1997, 3-8 Aug 1997). *Optimization of SAR interferogram by using coherence information.* Paper presented at the Geoscience and Remote Sensing, 1997. IGARSS '97. Remote Sensing - A Scientific Vision for Sustainable Development., 1997 IEEE International.

Zhao, C.-y., Zhang, Q., Yang, C., & Zou, W. (2011). Integration of MODIS data and Short Baseline Subset (SBAS) technique for land subsidence monitoring in Datong, China. *Journal of Geodynamics, 52*(1), 16-23.

Zhengxiao, L., & Bethel, J. (2008). *Image Coregistration in SAR Interferometry*. Paper presented at the The International Archieve of the Photogrammetry, Remote Sensing and Spatial Information Science.

APPENDIX: 1 (Field Observation)

X	Y	No	Structure	Disp	Trend	Dip	Lithology	Landcover/Morphology/Notes	Photo
219411	9922351	NA-01-11	fault scarp	vertical	N 0	86	volcanic tuff (weathered)	maize crops,settlement,grass,bush,undulating area	-
219198	9925397	NA-02-11	fault scarp	vertical	N 0	86		maize crop,schrubs,trees,grass,undulating area	-
220540	9929980	NA-03-11	fault scarp	vertical	N 0	86	volcanic tuff(weathered), pyroclastic	maize,settlement,nature vegetation,undulating area	NA-03-11
220893	9929989	NA-04-11				-		upper catchment,planted tress,undulating-hills	NA-04-11a
219921	9918887	NA-05-11	fault scarp	vertical	N 30 W	85	rhyolitic rocks,weathered tuff	rhyolites Quarry, undulating-hills	NA-05-11a,b,c
201407	9900697	NA-06-11	fault scarp	vertical	N 45 W	85	rhyolitic rocks,columnar joints	Fisher's Tower,Hell's Gate national park,undulating area	NA-06-11a,b,c,d
197902	9952775	NA-07-11	fault scarp	vertical	N 20 W	85	rhyolitic rocks (greyish, voggies)	shrubs,native vegetation, undulating-hills	
198633	9951926	NA-08-11	fault scarp	vertical	N 25 W	85	rhyolitic rocks	natural irrigation,hills, crops,native vegetation,hills,	NA-08-11
198722	9952024	NA-09-11				-	rhyolitic rocks	hot stream for fish pond,trees nursery,upper hills	NA-10-11
198799	9952166	NA-10-11				-	rhyolitic rocks	hot stream,upper hills	NA-11-11a,b,c,d
198775	9952185	NA-11-11	fault scarp	vertical (10m)	N 65 W	87	altered rhyolitic rocks,columnar joints,obsidians	hot spring, hot spring pond 10x5m(Majimoto),upper hills Gilgil	NA-12-11
200442	9901258	NA-12-11				-		Olkaria I, dewatering dam storage for injection wells	NA-13-11
200301	9900555	NA-13-11	fault scarp	vertical	N 25 W	85	ryholitic rocks, volcanic ash	undulating, hills	
200441	9901262	NA-14-11				-	altered rhyolitic rocks (grey-white),pumice,obsidians	Ololbutot Lava,undulating,hills	NA-14-11a,b,c,d,e
201401	9900872	NA-15-11	fault line	vertical	N 25 E	85	volcanic ash,tuff(white)	Ol Njorowa Gorge, valley	NA-15-11
201427	9900823	NA-16a-11	fault line	vertical	N 20 E	85	volcanic ash,tuff (white)	hot spring, Ol Njorowa Gorge,valley	NA-16-11a
201438	9900826	NA-16b-11	fault line	vertical	N 28 E	85	volcanic tuff(white)	Ol Njorowa Gorge,valley	NA-16-11b
201353	9900578	NA-17-11	fault line	vertical	N 40 E	85	intercalated layer of pyroclastics &tuff	Ol Njorowa Gorge,valley	NA-17-11
201903	9902255	NA-18-11	fault scarp	vertical (20m)	N 45 E	85	rhyolitic rocks,contact with volcanic tuff	hills	NA-18-11a,b,c
201945	9901238	NA-19-11				-	rhyolitic rocks	soliter hill	-
204456	9898206	NA-20-11				-		OW-912 (Olkaria Dome field),undulating,hills	-
204440	9901006	NA-21-11				-		Olkaria Dome Field, old craters,undulating,hills,Manyatta Village	NA-21-11a,b
202750	9902592	NA-22-11	fault scarp	vertical	N 45 E	85	ryholitic rocks, volcanic ash	hills, steep slope	NA-22-11
203692	9902868	NA-23-11	fault scarp	vertical	N 60 W	85		hills, steep slope	NA-23-11

204681	9902390	NA-24-11	fault scarp	vertical	N 60 W	85		hills, steep slope	-
205821	9904947	NA-25-11	fault scarp	vertical (15m)	N 40 E	85	rhyolitic rocks,columnar joints	hills, steep slope	NA-25-11a,b
205548	9905353	NA-26-11	fault scarp	vertical	N 35 W	85	rhyolitic rocks,columnar joints	hills, steep slope	NA-26-11
200774	9905436	NA-27-11				-	volcanic ash	uphills,sparse nature vegetation	-
201605	9905813	NA-28-11	fault scarp	vertical	N 45 W	85	volcanic ash	undulating areas, hills	-
201173	9905904	NA-29-11	fault scarp	vertical	N 45 W	85	volcanic ash	undulating areas, hills	NA-29-11
200924	9905630	NA-30-11	fault scarp	vertical	N 45 W	85	altered rhyolitic rocks,volcanic ash,obsidians	undulating areas, hills	NA-30-11
200889	9905582	NA-31-11	fault scarp	vertical	N 40 W	85	pyroclastic,intercalated with volcanic ash(30-50cm)	undulating areas, hills	NA-31-11
200683	9904429	NA-32-11				-	volcanic ash	undulating areas, hills	NA-32-11
200701	9904206	NA-33-11	fault line(infered)	vertical	N 45 E	85	volcanic ash	geothermal pipes	-
197755	9904923	NA-34-11	fault line(infered)	vertical	N 20 E	85	fumaroles,altered rhyolitic rocks,sulphur(yellowish)	undulating areas, hills	NA-34-11a,b,c
198080	9905061	NA-35-11				-		GPS point, G 26 X (geodetic point by Kenya Wildlife Service)	NA-35-11
196854	9902557	NA-36-11				-	altered rhyolitic rocks(white-yellowish),obsidians	Footslope Olkaria Hill,bush, shrubs,native vegetation	-
197286	9902893	NA-37-11	fault line(infered)	vertical	N 25 E	85	altered rhyolitic rocks(white), pyroclastic tuff, obsidians	undulating areas, hills	NA-37-11a,b,c
197819	9903781	NA-38-11	fault line(infered)	vertical	N 25 E	85	fumaroles,altered rhyolitic rocks,sulphur(yellowish)	undulating areas, hills	NA-38-11a
207000	9906195	NA-39-11				-		GPS point, Kenya Wildlife Service, Hell's Gate National Park	-
197603	9950386	NA-40-11				-	altered volcanic tuff(white-yellowish)	undulating area,bush,native vegetation	-
197943	9951275	NA-41-11	fault scarp	vertical	N 45 E	80	rhyolotic rocks	maize crops,undulating area	-
202286	9952888	NA-42-11	fault scarp	vertical (20m)	N 45 W	85	altered rhyolitic rocks, pumices,obsidians	shrubs, planted trees,undulating area	NA-42-11b
203092	9953230	NA-43-11	fault scarp	vertical	N 45 W	85	rhyolitic rocks	steep slopes,hills	NA-43-11a
202562	9953964	NA-44-11	fault scarp	vertical (10m)	N 65 W	86	rhyolitic rocks	Upper Gilgil river,steep slopes	NA-44-11
203135	9949922	NA-45-11	fault scarp	vertical (50m)	N 10 E	85	rhyolitic rocks	steep slopes	-
203229	9948903	NA-46-11	fault scarp	vertical	N 10 W	85	rhyolitic rocks	undulating area,shrubs, farms,protected forests	-
204759	9929775	NA-47-11	fault scarp	Vertical (10m)	N 20 E	85	rhyolitic rocks	bush, shrubs,native vegetation,steep slopes	NA-47-11a

203698	9928925	NA-48-11	fault scarp	vertical (15m)	N 45 W	89	rhyolitic rocks, columnar joints	undulating areas	-
203646	9928645	NA-49-11	fault scarp	vertical	N 25 E/ 65 W	85	rhyolitic rocks	swallow cave/nest, phosphate,undulating areas	NA-49-11a
203159	9928327	NA-50-11					rhyolitic rocks,columnar joints	undulatinga areas	NA-50-11
197698	9908918	NA-51-11						benchmark BM 18, Oserian Farm,undulating areas	NA-51-11
194777	9914778	NA-52-11						benchmark BM 24, Crater Lake, flat areas	NA-52-11
207667	9968133	NA-53-11	fault scarp	vertical	N 30	80	altered ryholitic rocks (yellowish-brown)	maize&weed crops,undulating	
212145	9964659	NA-54-11					altered rhyolitic rocks	weed&maize crops,malewa river,undulating-flat areas	